

---

This is an electronic reprint of the original article.  
This reprint may differ from the original in pagination and typographic detail.

Hao, Rui; Lin, Weiwei

## Evolution of surface roughness of notched steel details under fatigue loading

*Published in:*  
Structures

*DOI:*  
[10.1016/j.istruc.2023.105441](https://doi.org/10.1016/j.istruc.2023.105441)

Published: 01/12/2023

*Document Version*  
Publisher's PDF, also known as Version of record

*Published under the following license:*  
CC BY

*Please cite the original version:*  
Hao, R., & Lin, W. (2023). Evolution of surface roughness of notched steel details under fatigue loading. *Structures*, 58, Article 105441. <https://doi.org/10.1016/j.istruc.2023.105441>

---

This material is protected by copyright and other intellectual property rights, and duplication or sale of all or part of any of the repository collections is not permitted, except that material may be duplicated by you for your research use or educational purposes in electronic or print form. You must obtain permission for any other use. Electronic or print copies may not be offered, whether for sale or otherwise to anyone who is not an authorised user.



# Evolution of surface roughness of notched steel details under fatigue loading

Rui Hao, Weiwei Lin\*

Department of Civil Engineering, Aalto University, Espoo 02150, Finland

## ARTICLE INFO

### Keywords:

Fatigue of steel  
Fatigue crack initiation  
Surface roughness evolution  
Surface treatment  
Load ratio

## ABSTRACT

A fatigue crack initiates on the surface of the steel members, which can be attributed to the extrusions and intrusions caused by cyclic loading. The surface roughness parameters, including the statistical surface roughness and maximum surface roughness parameters, can characterize the increase in extrusion and intrusion. Six notched specimens were loaded with cyclic loading, and the evolution of the surface roughness parameters was monitored during the test to explore the characteristics of the surface roughness during the fatigue loading procedure in the high-cycle fatigue regime and clarify the effects of the initial surface finish and load ratio on the surface roughness evolution. Based on the test results, it was found that the 3D average surface roughness  $S_a$  and 3D root-mean-square surface roughness  $S_q$  were preferable for detecting the onset of fatigue cracks compared with the 2D average surface roughness  $R_a$  and 2D root-mean-square surface roughness  $R_q$ . The 3D maximum valley depth,  $S_v$ , was an effective indicator of the fatigue crack initiation location, except for compression-dominant fatigue loading. The evolution patterns of the 3D average surface roughness,  $S_a$ , and 3D root-mean-square surface roughness  $S_q$  during fatigue loading can be classified into three phases: instant response, damage accumulation, and crack-induced response. In addition, surface polishing is recommended for evaluation using 2D surface roughness parameters. However, it is not mandatory for evaluations using 3D surface roughness parameters. The effects of typical load ratios (0.1, -1, and 10) on the evolution pattern of the 3D statistical surface roughness parameters, especially in the instant response phase, were also investigated.

## 1. Introduction

Fatigue cracks are frequently observed in steel structures; they significantly decrease their service life and may even result in severe catastrophes [1]. In general, the initiation of fatigue cracks is due to the formation of a persistent slip band (PSB) on the surfaces of steel members subjected to a large number of repeated loads [2–3]. The occurrence of PSB is due to the extrusion of the surface profile, and the extrusion part cannot recover because of the oxidation reaction with air, resulting in plasticity deformation [23]. Simultaneously, intrusions occurred and developed with cyclic loading. Under such a mechanism, the stress concentration will increase on the surface, and finally, a microcrack is initiated at one intrusion site. When tracing back to the initiation mechanism of the fatigue crack, that is, the occurrence and evolution of the PSB, the direct result is a surface profile change, which the surface roughness parameters can quantitatively evaluate. It is reasonable to correlate fatigue behavior with surface roughness.

Several studies have been conducted to explore the practical

applicability of fatigue crack characterization using the concept of surface roughness. Itoga et al. [4] performed rotary-bending fatigue tests on high-strength steel specimens polished under four initial surface roughness conditions. They concluded that surface roughness only affects the fatigue life if the fatigue cracks initiate on the material surface, whereas it has little effect on the fatigue life in cases where fatigue cracks initiate below the material surface. The transition stress, i.e., the fatigue limit below which subsurface cracks occur in the fatigue procedure, is then quantitatively predicted with surface roughness parameters based on their experimental results by taking the surface roughness as notches. Alang et al. [5] conducted single-cantilever rotating-bending fatigue tests for three groups of carbon steel specimens with different initial surface roughness conditions and found that the fatigue lives of specimens with lower initial surface roughness conditions were higher than those of specimens with higher initial surface roughness conditions. In addition, fatigue fractures were observed to initiate and propagate in a transgranular manner. Saberifar et al. [6] studied the effects of non-metallic inclusions and surface roughness on fatigue life using the

\* Corresponding author.

E-mail address: [weiwei.lin@aalto.fi](mailto:weiwei.lin@aalto.fi) (W. Lin).

<https://doi.org/10.1016/j.istruc.2023.105441>

Received 22 December 2022; Received in revised form 16 October 2023; Accepted 21 October 2023

Available online 8 November 2023

2352-0124/© 2023 The Author(s). Published by Elsevier Ltd on behalf of Institution of Structural Engineers. This is an open access article under the CC BY license (<http://creativecommons.org/licenses/by/4.0/>).

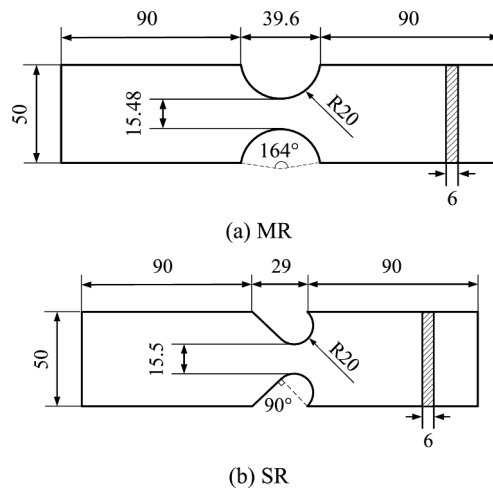


Fig. 1. Geometry of two types of specimens (unit: mm).

Table 1  
Test specimens.

Series	Surface finish	Load ratio R	Notch root radius/ mm	Fatigue load/kN	
				minimum	maximum
MR-U	unpolished	0.1	20	3.72	37.2
MR-P	polished	0.1	20	3.72	37.2
SR-U	unpolished	0.1	10	3.44	34.4
SR-P-1	polished	0.1	10	3.44	34.4
SR-P-2	polished	-1	10	-15.48	15.48
SR-P-3	polished	10 (-5)	10	-34.4 (-25.8)	-3.44 (5.16)

experimental results of rotating–bending fatigue tests for two groups of 30MnVS6 specimens with different inclusion sizes and initial surface roughness conditions. This study concluded that fatigue damage occurs at locations where large non-metallic inclusions exist, and both non-metallic inclusions and surface roughness act as stress intensifiers that decrease the fatigue strength of the materials. Lai et al. [7] proposed a unified model for predicting S-N properties such as the upper and lower limits, and the model considered the effect of surface roughness by treating the surface groove as a notch and employing fracture mechanics. Similar to Itoga [4], fatigue cracks tend to initiate at subsurface

non-metallic inclusions in smooth specimens, whereas fatigue crack initiation occurs on free surfaces in rough specimens. For traditional metallic materials and additive manufacturing components, surface roughness also plays an important role in fatigue behavior. Gockel et al. [8] found that the maximum pit height, a surface roughness parameter, affects the fatigue life of additive-manufactured alloy 718. By contrast, Shrestha et al. [9] drew a distinct conclusion. They performed uniaxial fatigue tests for laser beam powder bed fusion (LB-PBF) additive of 316 L stainless steel rod specimens with cylindrical shapes. In the fatigue tests, the specimens were classified into two categories (as-built surface conditions with two different fabrication orientations) and loaded using a strain control method. They found that surface roughness had little effect on the fatigue life of LB-PBF 316 L stainless steel. This indicates that the relationship between the surface roughness and fatigue behavior differs from material to material.

In addition to discussing the relationship between surface roughness

Table 2  
Material properties of the steel.

Steel grade	Yield strength	Tensile strength	Elastic modulus
S355	405.9 MPa	481.95 MPa	211 GPa

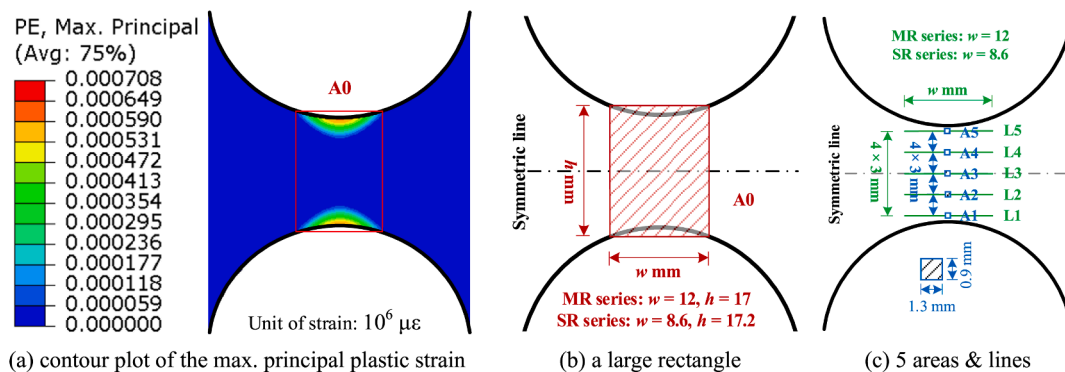


Fig. 2. Selected regions for surface roughness measurement.



(a) surface roughness measurement



(b) fatigue test

Fig. 3. Experimental setup.

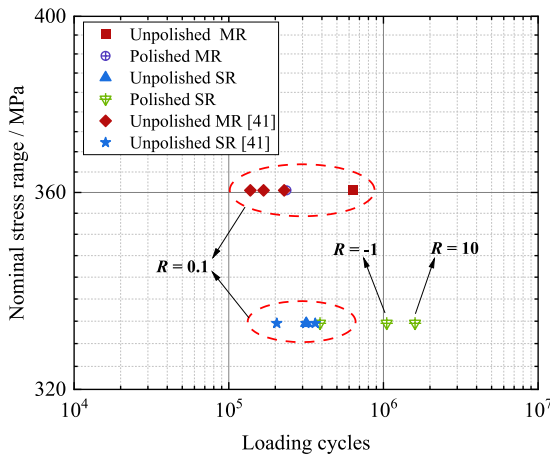


Fig. 4. S-N plots of the fatigue test results.

Table 3  
Definitions of surface roughness parameters.

Description	2D	3D
Arithmetic average of profile height deviations from the mean line (2D) or plane (3D)	$R_a = \frac{1}{L} \int_0^L  z(x)  dx$	$S_a = \frac{1}{A} \iint_A  z(x,y)  dx dy$
Quadratic average of profile height deviations from the mean line (2D) or plane (3D)	$R_q = \sqrt{\frac{1}{L} \int_0^L z^2(x) dx}$	$S_q = \sqrt{\frac{1}{A} \iint_A z^2(x,y) dx dy}$
Maximum peak height above the mean line (2D) or plane (3D)	$R_p = \max(z(x))$	$S_p = \max(z(x,y))$
Maximum valley depth below the mean line (2D) or plane (3D)	$R_v = \min(z(x))$	$S_v = \min(z(x,y))$

and fatigue behavior, studies have been performed to investigate surface roughness-based fatigue life prediction. Maiya and Busch [10] quantitatively studied the relationship between the fatigue crack initiation life and the surface roughness parameter for hourglass-shaped specimens of type 304 stainless steel and established a power equation for the fatigue crack initiation life in terms of the root mean square (RMS) roughness parameter. Xiao et al. [11] performed low-cycle fatigue tests of 34 dumbbell specimens that were divided into ten groups with different surface roughness varying from 0.1 μm to 1.7 μm. From the results, a power equation between the surface roughness parameter and fatigue life was proposed, and a qualitative interpretation of this equation was provided by correlating the surface roughness parameters and the stress concentration factor. In contrast to the empirical methods used in [10,11], Wang et al. [12] and Li et al. [13] employed the Tanaka and Mura model, which correlates surface crack initiation to slip band dislocation movement, to predict the fatigue crack initiation life of FV520B-I stainless steel and medium-carbon steel, respectively. Surface roughness parameters were used to calculate the relevant parameters in the Tanaka and Mura models.

Despite the interesting findings between surface roughness and fatigue behavior of metallic materials, it is still difficult to directly apply these outcomes to engineering structures. A major requirement for engineering structures is the detection of fatigue cracks during early stages. As the fatigue crack initiates from the PSB, that is, the initiation of the fatigue crack occurs on the surface of the specimens [17], surface measurements can be conducted to detect the onset of fatigue cracks. However, despite the many available detection methods, detecting fatigue cracks is often difficult because of the elusive initial size and crack closure phenomenon caused by compressive action. For example, the eddy-current method can be used to detect a minimal crack size of approximately 3–4 mm [14]. Since the widely adopted initial crack length is from 1 μm to 1 mm [15], however, it cannot detect the initial fatigue cracks. Therefore, monitoring surface roughness evolution is a potential fatigue assessment method for studying the fatigue process and has drawn the attention of scholars in recent decades [16]. In Ogawa and Hatanak's work [18], atomic force microscopy (AFM) was used to measure the surface roughness evolution for a JIS S45C rod specimen during a tension–compression cyclic loading with load ratio  $R = -1$ , and the increase of surface roughness with fatigue loading cycles was

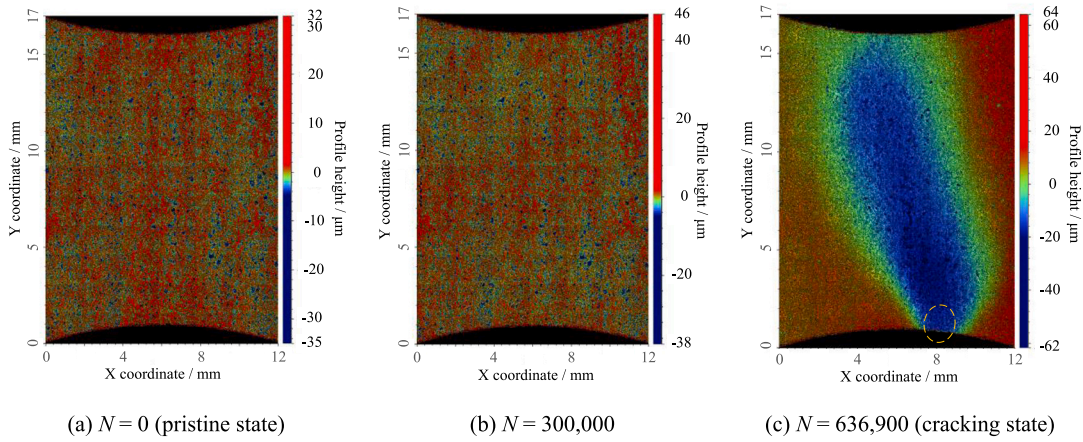


Fig. 5. Contour plots of the surface profile of MR-U at different loading cycles.

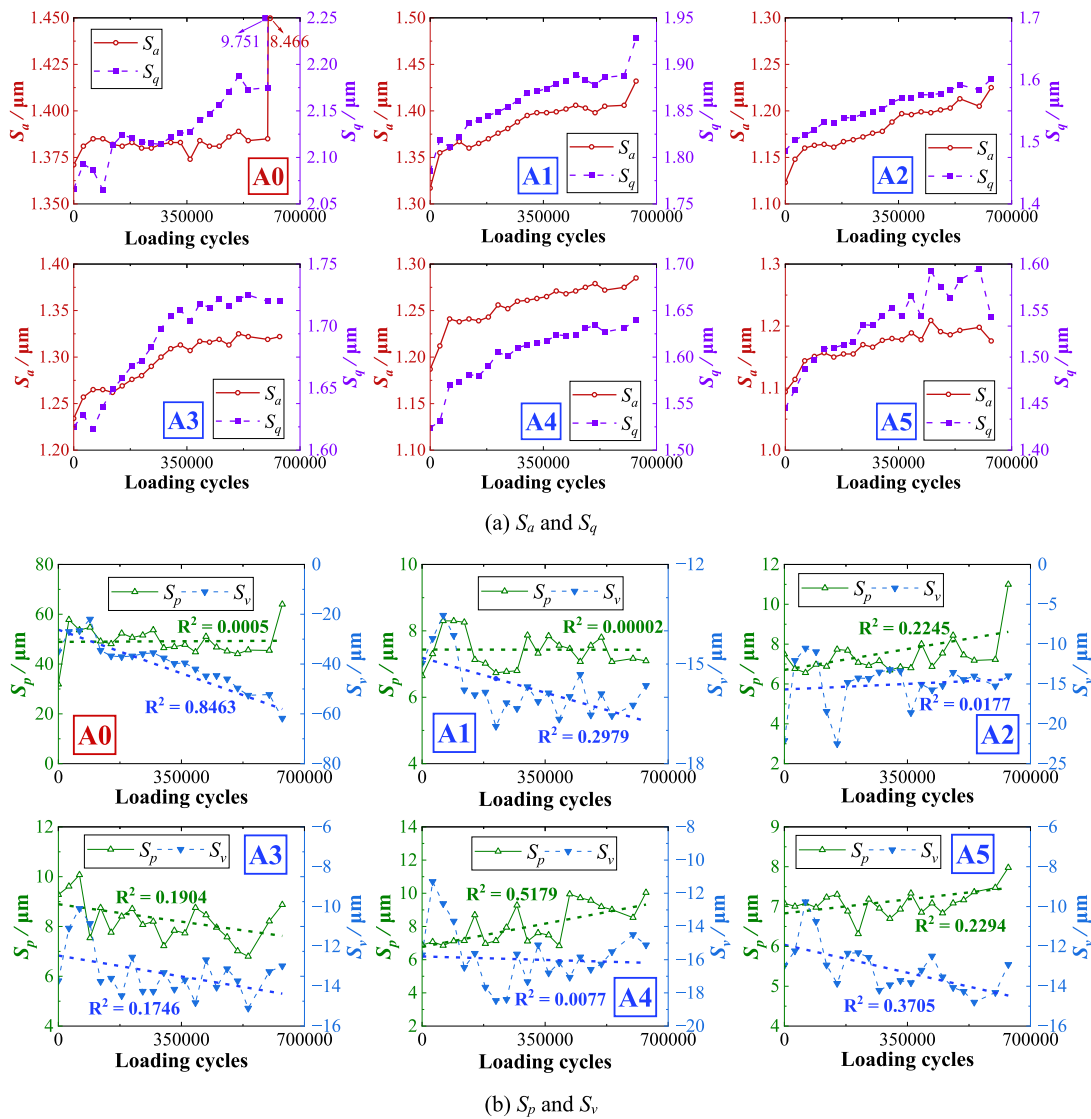


Fig. 6. Evolution of 3D parameters for MR-U.

observed. In addition, they observed an increasing surface roughness rate and found that the rate was high at the early stage of fatigue loading and decreased later with an increase in the number of loading cycles.

Yue [17] employed a rate-dependent crystal plasticity model to establish a finite element model containing 250 aluminum grains to simulate 176 fatigue load cycles and observed that the surface roughness parameter

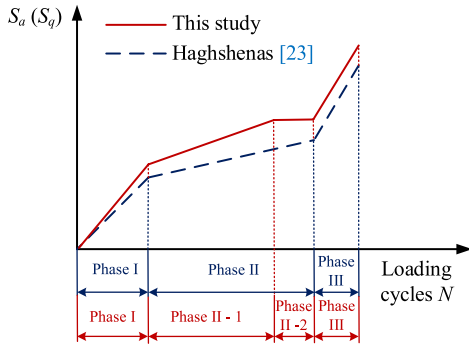
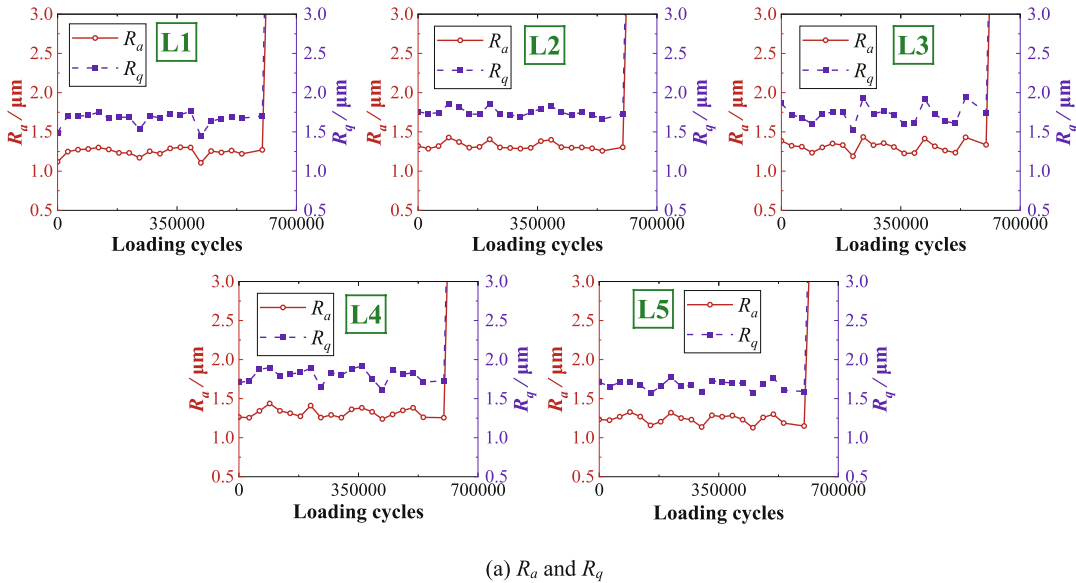


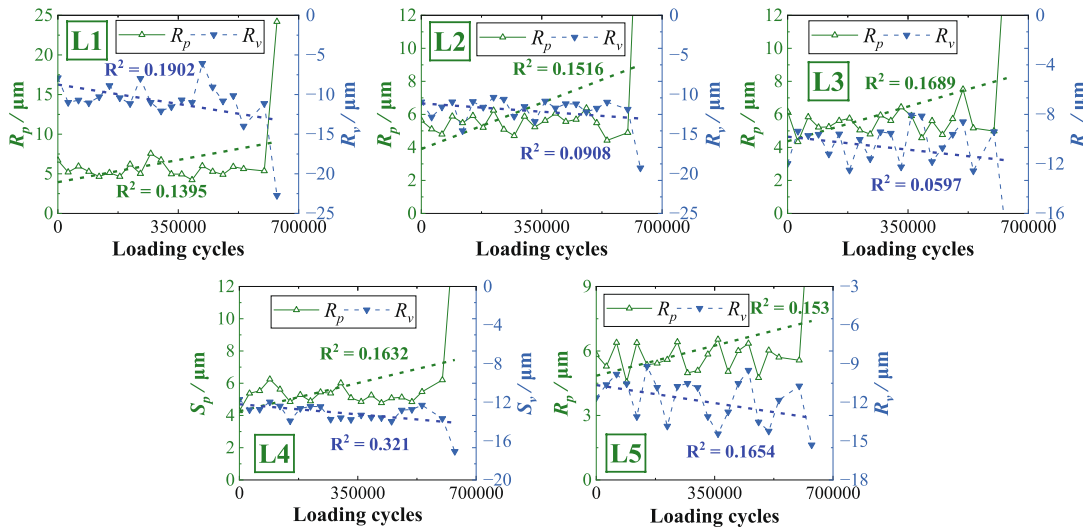
Fig. 7. Evolution patterns of  $S_a$  and  $S_q$ .

increased with loading cycles. Hussein et al. [19] established 3D discrete dislocation dynamics models for single crystals with different sizes and initial dislocation densities under axial fatigue loading and confirmed that the surface roughness increases with loading cycles, and the changing rate increases with crystal size. Wang et al. [20] found that in a

low-cycle fatigue (LCF) loading procedure, the surface roughness increased with the loading cycles and stress levels, and the occurrence of out-of-plane grain displacement was also explained. Lacerda et al. [21] observed the microstructural intrusions and extrusions of the surface of SAE 1020 steel specimens under three fatigue load levels. They proposed using the ratio of the inclination of the evolution curves of the peaks and valleys to predict fatigue failure. Tada and Uemori [22] experimentally studied the microscopic surface deformation of a pure titanium plate specimen subjected to cyclic tension loading, and the surface height change, that is, the elastic and plastic deformation of surface grains, was measured. The mechanism by which the surface grains undergo rise and sink deformations during the cyclic loading procedure was explained and attributed to the effect of the geometries and crystal orientations of the subsurface grains. Haghshenas and Khonsari [23] monitored the surface roughness evolution during fatigue loading for specimens with different surface finishes and found that the feasible and sensitive surface roughness parameter characterizes the initiation of fatigue cracks. In addition, a relationship between the critical surface roughness parameter and the stress level was proposed. Sola et al. [24] performed a fatigue test on a nickel plate specimen with intermittent surface topology measurements during the test. The surface topology was obtained



(a)  $R_a$  and  $R_q$



(b)  $R_p$  and  $R_v$

Fig. 8. Evolution of 2D parameters for MR-U.

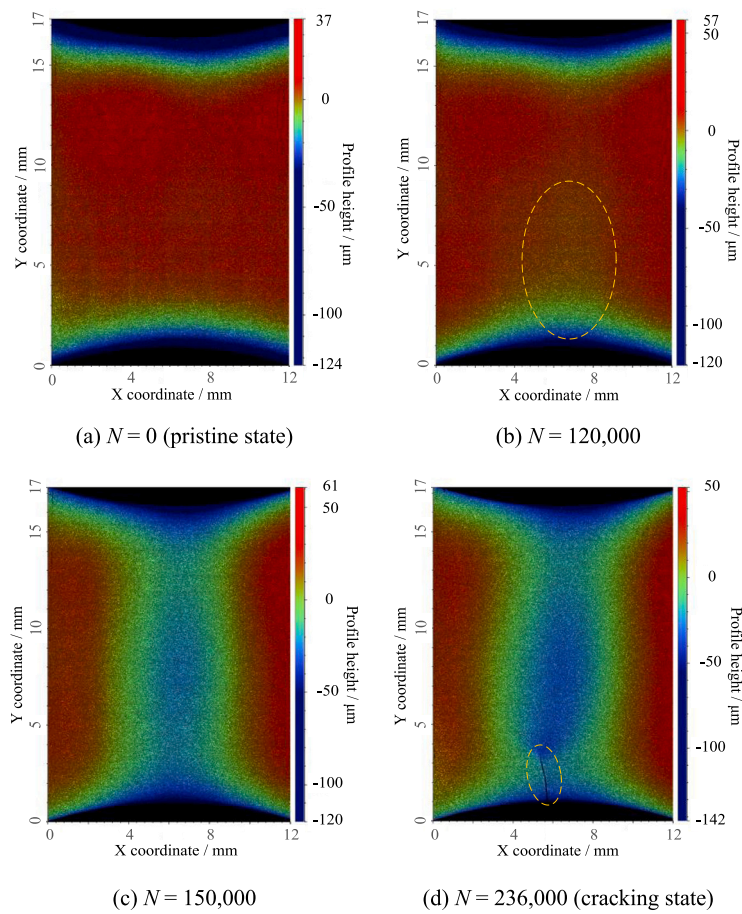


Fig. 9. Contour plots of the surface profile of MR-P at different loading cycles.

using scanning white light interferometry (SWLI), and the surface roughness changes were evaluated using an image registration technique. According to the results, they observed that the heights of the slip bands increased with the loading cycles, and a surface roughness parameter-based fatigue damage initiation prediction was proposed. In addition to studying the evolution of the surface roughness before fatigue crack initiation, attention was paid to the changes in the surface roughness during fatigue crack propagation. Kelton et al. [25] investigated the relationship between the change in the surface roughness and the growth of the plastic zone around the crack tip of a fatigue crack when it was pinned and released to propagate. In this study, a nickel center-notch specimen was subjected to fatigue loading, and the surface roughness change at the crack tip was monitored. When the fatigue crack was pinned, they observed a considerable surface roughness change within the cyclic plastic zone around the crack tip. After the fatigue crack was released from the pinned state, a significant surface roughness change occurred within the monotonic plastic zone.

This study uses a local structural detail in steel bridges as the research object: a cutout, which is a notch in shape that exhibits obvious notch effects when subjected to actual traffic loads. Some fatigue cracks initiated from cutouts in existing bridges propagated to a considerable size when initially observed, which means that a fatigue crack detection method capable of early detection is preferable for engineering practices. A material-level behavior investigation is necessary to achieve such early detection because fatigue cracks are essentially local damage initiated from PSBs in surface grains, which is too subtle to be captured by structural measurements. Material-level fatigue damage investigation helps in understanding the damage mechanism. In particular, laboratory steel coupons can reproduce the dominant stress state for cutout details in steel bridges, resembling the real situation. According to the

mentioned relationship between fatigue and surface topology changes and the results obtained in [23], the surface roughness-based method may be a potential solution to our research objective. However, the fatigue occurring at the cutout can be classified as high-cycle fatigue (HCF), and the fatigue mechanism is different from that of LCF, which is the mainstream literature on this topic. In addition, structural steel used in civil engineering has different material properties from the materials employed in the available literature, and the evolution pattern of the surface roughness during the fatigue loading procedure may differ from material to material, making it necessary to conduct high-cycle fatigue tests with surface roughness monitoring during the fatigue loading process. Another noteworthy question is whether surface treatment (e.g., polishing) is preferable before measuring the surface roughness of the structural details despite changes to the initial surface finishing state. Although it has been reported that surface finishing comprehensively affects the fatigue life of a fatigued member [26,27], the effects of surface finishing on the surface roughness evolution are still unclear. In addition, some fatigue-prone structural details experience complex stress histories (even those dominated by compressive stress [28]), resulting in load ratios that differ from those under most laboratory conditions. Although the effects of the load ratio on fatigue life have been studied by Xin [29], its effects on surface roughness evolution have not yet been investigated [20]. Against this background, this study aimed to investigate the effects of different initial surface finishing states and load ratios on the evolution of surface roughness during fatigue loading. A sampling region (observed area) should be specified when the surface roughness is measured. However, a clear recommendation for deciding the dimensions of the sampling regions is not available. Therefore, this study also discusses the effect of the sampling region on the surface roughness

measurements. The results of this pilot study can provide a reference for in situ fatigue crack detection, where surface roughness is employed as an indicator.

## 2. Description of the test

### 2.1. Specimen design and preparation

To explore the applicability of surface roughness monitoring in the field of bridge engineering, particularly for steel bridges, two dog-bone-like specimens were designed based on the observed fatigue cracks in real bridges [30,31], as shown in Fig. 1. Similar notched details are widely applied in the cutouts of rib-to-floor beam connections in orthotropic steel bridges [32–35] and ship engineering, for example, the corner of the balcony opening of a cruise ship [36]. Fatigue cracks are prone to initiate at these notched details. Another goal of such a design is to compare the differences in the surface roughness evolution at different stress levels. For convenience, specimens with radii of 20 mm and 10 mm were designated as medium radius (MR) and small radius (SR), respectively.

Table 1 shows a summary of the specimens used in this study. A total

of six specimens were manufactured using the waterjet cutting method. Among these specimens, the main varying parameters are the initial surface finishing and load ratio. Four specimens were polished with sandpapers P120, 240, 320, 400, 600, 800, and 1200 in sequence to study the effect of the initial surface finish on the evolution of the surface roughness while the remaining two specimens remained in their pristine state. Three load ratios, 0.1, -1, and 10 were set to study the effect of load ratio on the surface roughness evolution, and they represent the tension-tension, tension-compression, and compression-compression, respectively. In particular, a load ratio of 10 was selected because the stress status near the critical notched detail remained almost compressive during the field measurement period, according to the data reported in [37]. Note that because SR-P-3 is always loaded with compressive force and this cannot enable the initiation of macro fatigue cracks, a load ratio of -5 (from -25.8 kN to 5.16 kN) is applied instead after 1 million cycles.

The measured material properties of the steel plate are listed in Table 2.

Fig. 2 illustrates the regions selected during the surface roughness measurement. Although the fatigue loads applied to the specimens caused the fatigue life to lie in the HCF regime, local yielding occurred

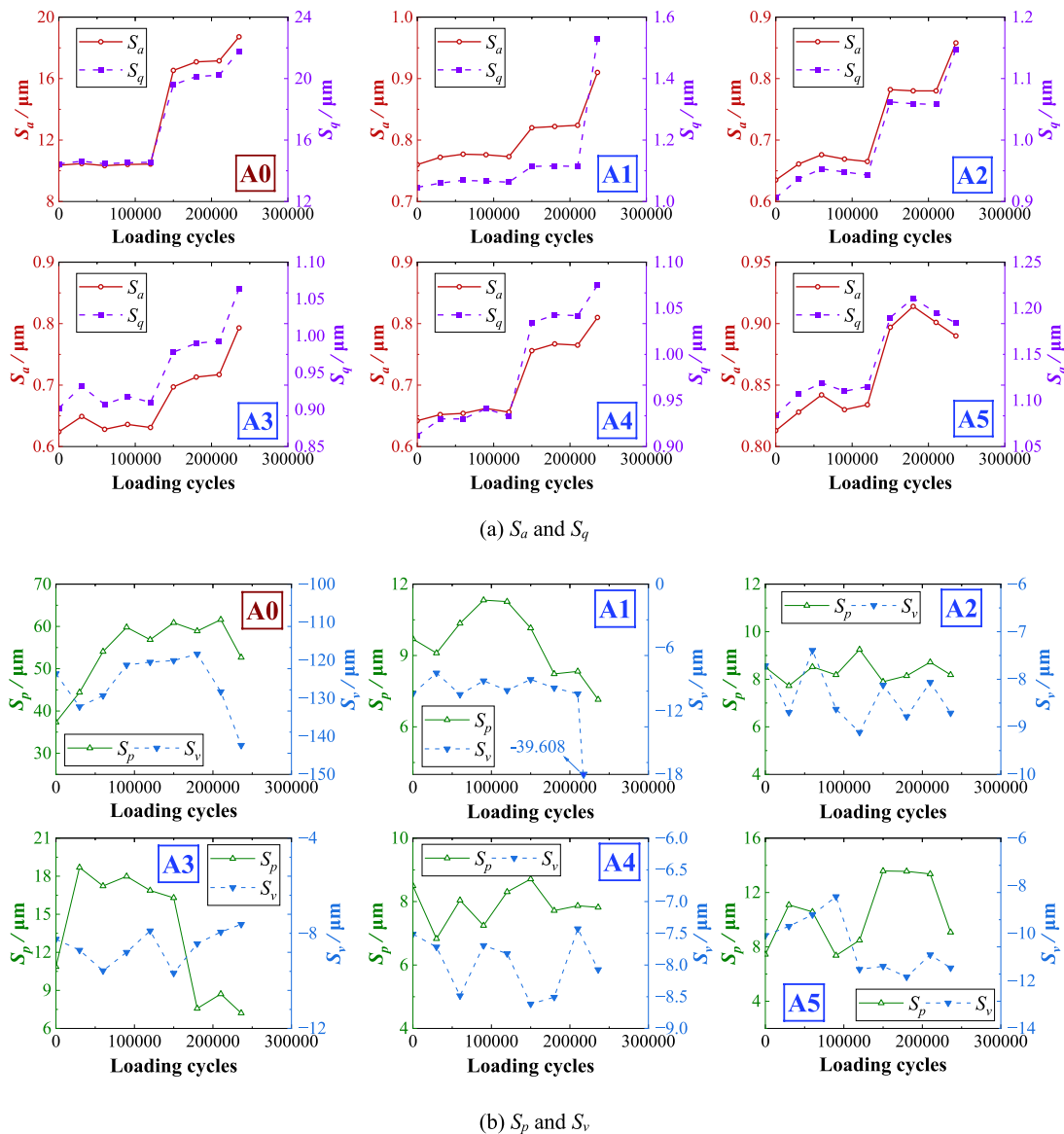


Fig. 10. Evolution of 3D parameters for MR-P.

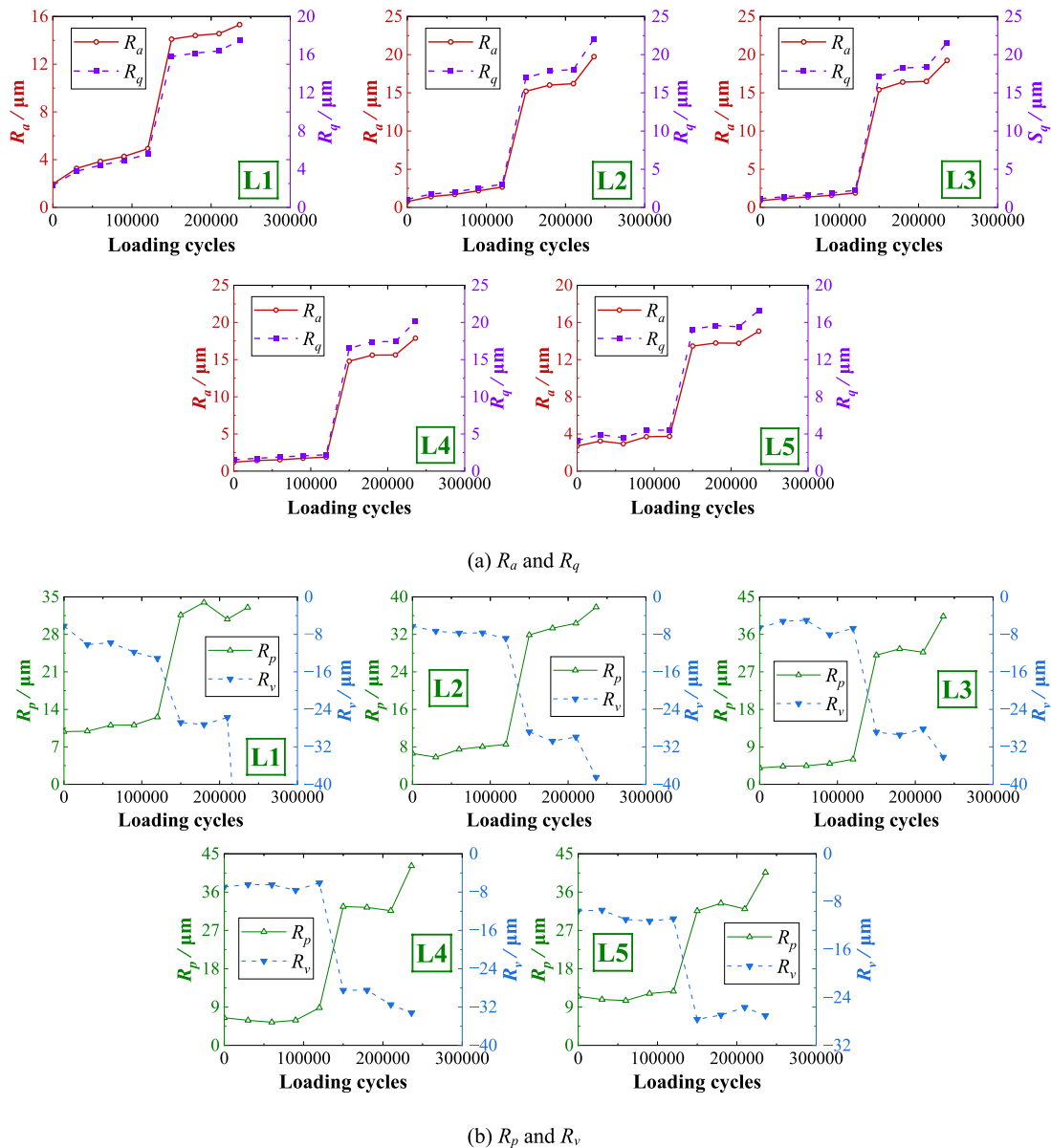


Fig. 11. Evolution of 2D parameters for MR-P.

when the cyclic load approached its maximum value. Preliminary elastoplastic finite element (FE) analyses were performed using ABAQUS to ensure that the fatigue crack could be captured. The FE model was statically loaded with the maximum cyclic loads listed in Table 1, and the material properties listed in Table 2 were employed. The C3D8R element was used in the FE model, and the boundary conditions were based on the actual conditions in the fatigue test. The mesh near the notch root was approximately 0.125 mm, and a mesh sensitivity analysis was conducted [41] to obtain convergent results. Taking the MR series as an example, the maximum principal plastic strain (PE, Max. Principal) is presented in Fig. 2(a). Then, the rectangular area in Fig. 2(b) was selected such that area A0 covered the local yield zone predicted by the FE analyses, and five typical areas and lines in Fig. 2(c) were selected to investigate the effects of the stress level. Notably, the 2D surface roughness parameters shown in Fig. 2(c) were extracted from the measurement results of A0.

### 2.2. Fatigue test procedure

For each specimen, the initial surface roughness was first measured. Then, the specimen was mounted to be loaded with cyclic loading for several cycles (30,000 cycles in most cases), after which the specimen was unmounted and sent back for measurement by the interferometer. These steps were repeated until a fatigue crack was formed.

The surface roughness measurement was conducted using the BRUKER ContourGT InMotion White Light Interferometer, which enables accurate measurement of 0.1 nm in the height direction and lateral resolution up to 380 nm, as shown in Fig. 3(a). Compared to the magnification factor of  $2.75\times$  when measuring area A0, a scope with a slightly higher magnification factor of  $5\times$  was used when measuring areas A1–A5. Due to the difference in magnification factor, the lateral resolution for areas A1 to A5 is around 1  $\mu\text{m}$ , while for A0, it is around 3  $\mu\text{m}$ .

Fig. 3(b) shows the experimental setup of the fatigue test, in which the fatigue testing machine MTS 810 (loading capacity: 100 kN) was used. A constant amplitude sinusoidal loading was applied for each

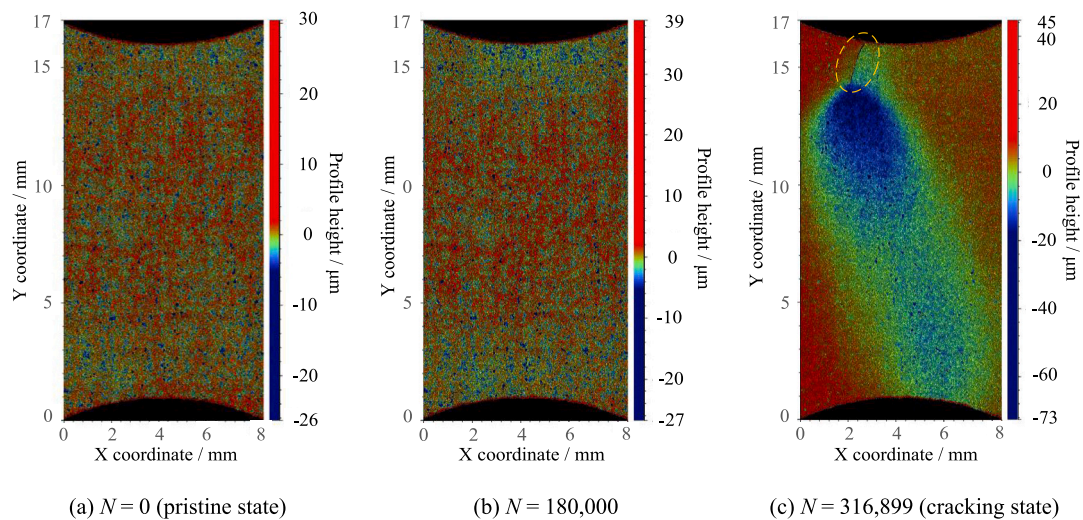


Fig. 12. Contour plots of the surface profile of SR-U at different loading cycles.

specimen with a load ratio of  $R = 0.1$  (also  $-1$  and  $10$  for series SR). The loading frequency was set to  $20$  Hz. Once the displacement range increased to  $1.25$  times the initial displacement range, which indicated fatigue crack initiation in the experiment, the fatigue loading was terminated, and the final surface roughness was measured.

### 3. Results and discussions

#### 3.1. Fatigue test results

As shown in Fig. 4, the log–log plot of the nominal stress ranges and fatigue lives of the specimens in this study is presented in Fig. 4. For comparison, previous fatigue test results [41] conducted by the authors on the same specimens are also plotted. It can be found that for the SR series (both polished and unpolished) with a load ratio of  $0.1$ , similar fatigue lives were obtained, and the unpolished SR specimen in this study also yielded similar fatigue lives to the ones in our previous test. But when it comes to the specimens with load ratios of  $-1$  and  $10$ , fatigue lives were greatly increased, which can be accounted for by the contribution of the compressive stress. For the MR series, the polished specimen in this test had a lower fatigue life than the unpolished specimen. This contradicts the common idea that polishing contributes to a higher fatigue life owing to the possible elimination of micro defects that can develop into long cracks. This may be because the polishing in this study did not cover the cut face of the specimen, where a fatigue crack might also be initiated. If a crack initiates from the cut face (or the cutting process introduces large initial defects to the cut face), then polishing may not enhance the fatigue life. However, the polished MR specimens had a longer fatigue life than all the unpolished MR specimens in our previous test.

#### 3.2. Surface roughness evolution results

The surface roughness evolution is presented by the evolution of relevant parameters frequently used in practice, and the definitions of these parameters [38] are given in Table 3. The surface parameters with subscripts  $a$ ,  $q$ ,  $p$ , and  $v$  represent the arithmetic average surface roughness, quadratic average surface roughness, maximum peak height, and maximum valley depth, respectively. The height of the surface profile  $z$  is based on the mean line (mean plane) system, in which the average value of all measured data points is equal to zero. Linear fit and plane fit were used in this study to determine the mean line (mean plane).

##### 3.2.1. MR-U

Fig. 5 shows the contour plots of the surface profile of the MR-U specimen at different loading cycles. With the loading cycles varying from  $0$  to  $30,000$ , the contour plot does not show any significant changes in terms of pattern, while the increasing of peak height (from  $32$   $\mu\text{m}$  to  $46$   $\mu\text{m}$ ) and the decreasing of valley depth (from  $-35$   $\mu\text{m}$  to  $-38$   $\mu\text{m}$ ) are observed. When a fatigue crack initiates on the other side of the specimen, the contour plot corresponding to the crack state (Fig. 5(c)) exhibits a large concavity that is caused by cracking and the subsequent decrease in the effective section, which can be seen as the most significant contributing factor to the surface roughness increase of A0 (see Fig. 6(a)).

Fig. 6 shows the evolution of the 3D roughness parameters for the MR-U specimen. The statistical surface roughness parameters  $S_a$  and  $S_q$  present a relatively clear evolution pattern compared with the other two maximum surface roughness parameters,  $S_p$  and  $S_v$ . This is because, as illustrated in Table 3, the definitions of  $S_a$  and  $S_q$  are in integral form, which can significantly weaken the effects of random factors in the measurement, such as dirt on the measured surface or the shifted position of the specimen between two different measurements. Similar to that reported in Haghshenas's research [23], the evolutions of the surface roughness parameters  $S_a$  and  $S_q$  show three phases (see Fig. 7): Phase I, a rapid rise owing to the first application of the fatigue load; Phase II, a steady increase with the loading cycles, and the increasing rate remains approximately constant; Phase III, another rapid rise triggered by the fatigue crack initiation. However, in some measurement areas, such as A1 and A4, a short plateau was observed at the end of Phase II. According to Meng [39], this was presumably because a saturation regime was reached after several cycles. In this regime, the heights of the extrusions and intrusions remain unchanged. However, the mechanisms underlying this short plateau require further investigation.

To evaluate the maximum surface roughness parameters  $S_p$  and  $S_v$  in this study, surface roughness measurements were conducted with the specimen mounted and demounted during the entire fatigue loading procedure, making the measured area slightly different among all the measurements. The zero plane and line in the surface roughness calculation are based on all data points, which makes the results sensitive to changes in the observed area. In addition, according to Tada and Uemori [22], the fluctuation in the measurement results can also be accounted for by the reversibility of slip deformation. Therefore, a linear regression method was used to obtain the evolution tendencies of these two parameters. The coefficient of determination  $R^2$  values for each linear fit equation for both  $S_p$  and  $S_v$  in the different measured regions are also

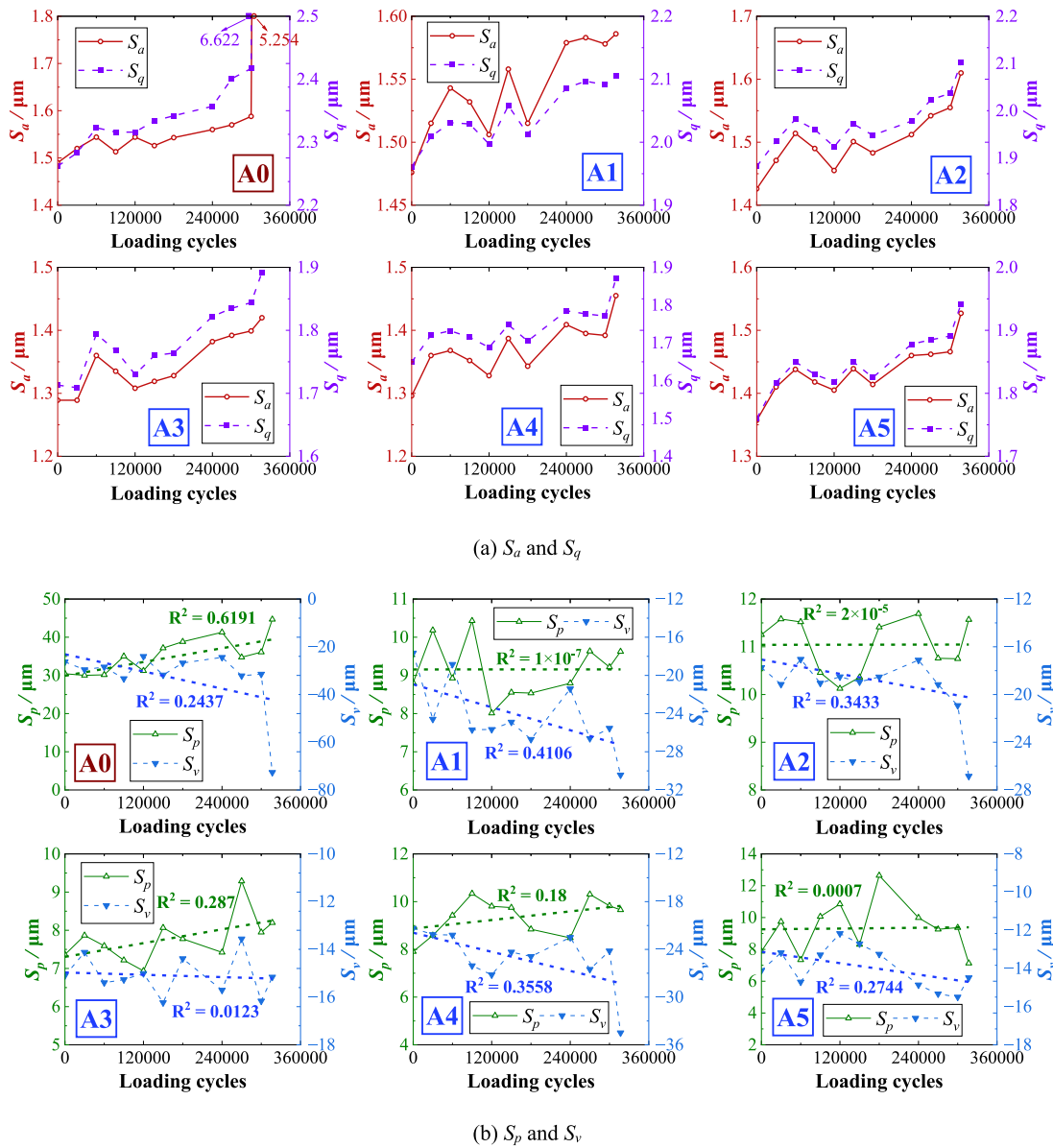


Fig. 13. Evolution of 3D parameters for SR-U.

presented in Fig. 6(b). At A1 and A5, where plastic deformation developed, the evolution of  $S_v$  had a stronger correlation with the loading cycles than  $S_p$ , whereas at A2 and A4, where no plastic deformation developed, the evolution of  $S_p$  had a stronger correlation with the loading cycles. This is compatible with the conclusion drawn in [23], which shows that  $S_v$  is more sensitive to fatigue damage accumulation in the LCF regime, while  $S_p$  shows more sensitivity to fatigue damage accumulation in the HCF regime.

Fig. 8 shows the evolution of the 2D roughness parameters for the MR-U specimen. These results show that, unlike  $S_a$  and  $S_q$ , no obvious damage accumulation is observed in  $R_a$  and  $R_q$  as the number of loading cycles increases, and the huge jump corresponding to the cracking state results from the emergence of a concavity triggered by the fatigue crack. A similar evolution in the damage-accumulation phase was also observed in  $R_p$  and  $R_v$ .

### 3.2.2. MR-P

Fig. 9 shows the contour plots of the surface profile of MR-P at different loading cycles. By comparing the surface profiles shown in Fig. 9(a) and (b), a concave shape was observed in the highly stressed

region when  $N = 120,000$ . From the contour plot corresponding to the cracking state, it can also be observed that there is a local concavity around the crack tip, which can be seen as the most significant contributing factor to the surface roughness increase of the A0. It is worth mentioning that during the fatigue test, an overload was accidentally applied to the specimen when the number of loading cycles reached 150,000, and then a necking-like region emerged.

Fig. 10 shows the evolution of the 3D roughness parameters for the MR-P specimen. It is clear that the accidental overload spikes the values of  $S_a$  and  $S_q$  at all measured areas, and the amount of change at A1 and A5 is around  $0.05 \mu\text{m}$ , which is lower than that of the other three areas. If the abrupt increase caused by accidental overload is ignored, the evolution patterns of  $S_a$  and  $S_q$  still follow a three-phase behavior, although the rapid increase in Phase I is not obvious at A1. This indicated that a large plastic deformation had a limited effect on the evolution patterns of  $S_a$  and  $S_q$ . As for  $S_p$  and  $S_v$ , a linear fit was not performed because the overload at 150,000 cycles significantly affects their values, as it could not yield reasonable results.

Fig. 11 shows the evolution of the 2D roughness parameters for the MR-P specimen. In contrast to MR-U, the damage accumulation of both

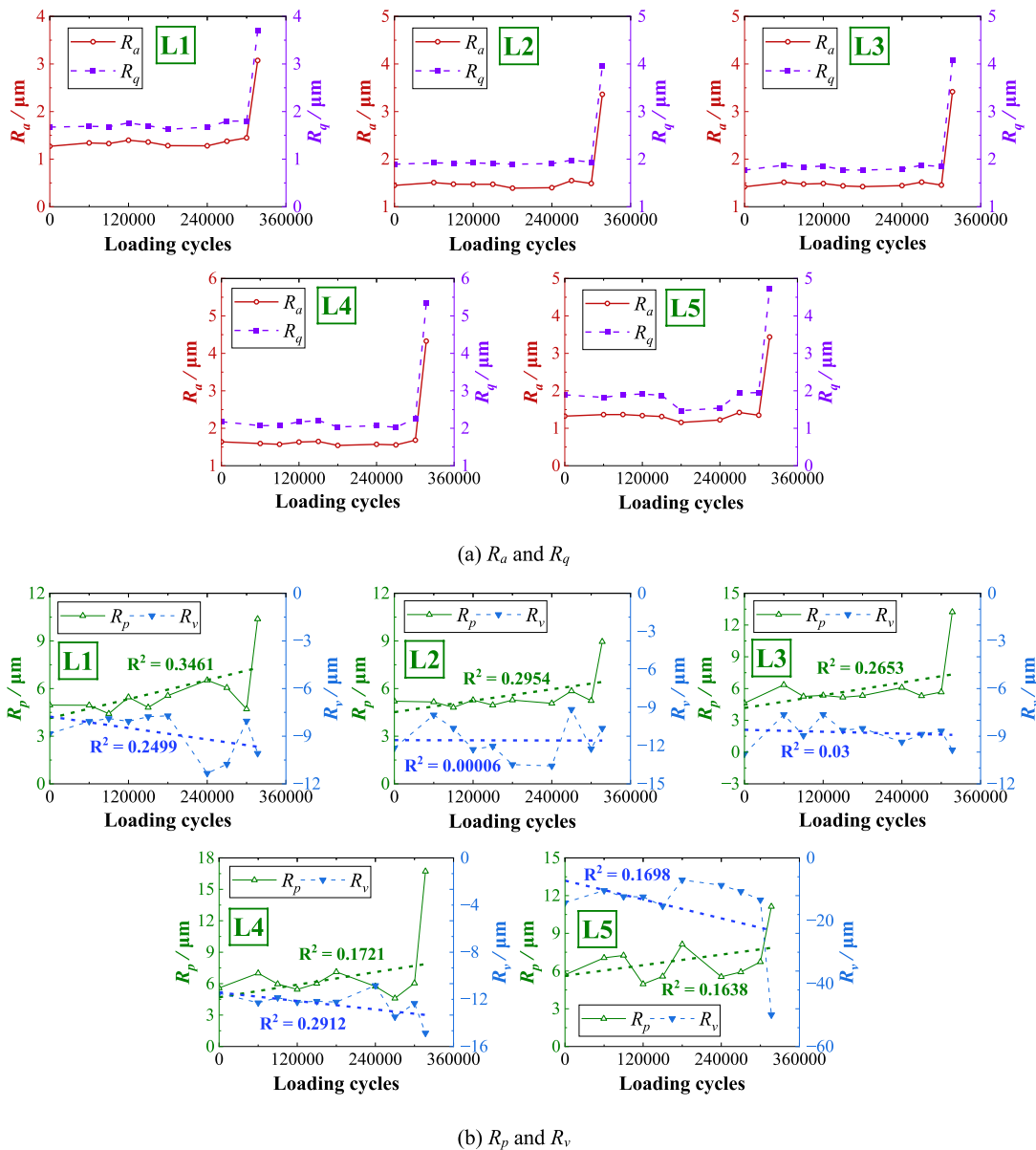


Fig. 14. Evolution of 2D parameters for SR-U.

$R_a$  and  $R_q$  is evident in MR-P; in particular, the evolution at L1 exhibits a clear, rapid increase in Phase I. Similarly, if the abrupt increase due to the accidental overload, which can be observed from 120,000 cycles to 150,000 cycles in Fig. 11 is ignored, the rate of change in the damage accumulation phase at all locations remains almost constant. This shows that the large plastic deformation limits the evolution pattern of  $R_a$  and  $R_q$ . Similar to  $S_p$  and  $S_v$ , no linear fit was obtained for  $R_p$  and  $R_v$ . However, before the overload, the evolutions of  $R_p$  and  $R_v$  at L1 show an increasing and decreasing tendency, respectively.

### 3.2.3. SR-U

Fig. 12 shows the contour plots of the surface profile of SR-U at different loading cycles. After being loaded for 180,000 cycles (from Fig. 12(a) and (b)), the surface within the highly stressed region, that is, the notch root, tended to drop. A large concave shape formed at the crack tip when a fatigue crack was initiated. In addition, there was an apparent height difference along the fatigue-crack propagation path.

Fig. 13 shows the evolution of the 3D roughness parameters for SR-U. A rapid increase was observed in the first loading interval (0–30,000

cycles) in all areas except A3. Several unexpected drops at  $N = 90,000$ , 120,000, and 180,000 were observed in the damage accumulation phase, which can be attributed to alignment errors among the different loading intervals. If these drops are ignored, the evolutions of  $S_a$  and  $S_q$  at A1, A2, A4, and A5 demonstrate three-phase behavior. In particular, a short plateau was observed at A1 and A4 from 240,000 to 300,000 cycles. By comparing the evolutions of  $S_p$  and  $S_v$  at A1 to A5, it was found that  $S_v$  had a stronger correlation with the loading cycles at all locations except A3, where the stress level was the minimum.

Fig. 14 shows the evolution of the 2D roughness parameters for SR-U. Similar to MR-U, no obvious damage accumulation was observed in  $R_a$  and  $R_p$  as the number of loading cycles increased, and the large jump corresponding to the cracking state resulted from the concavity triggered by the fatigue crack. When approaching the crack initiation location, that is, from L1 to L5, the correlation between  $R_v$  and the loading cycles increases, whereas for  $R_p$ , the opposite tendency is observed. This indicates that  $R_v$  is more sensitive to the fatigue loading cycles near where the fatigue crack is about to be initiated.

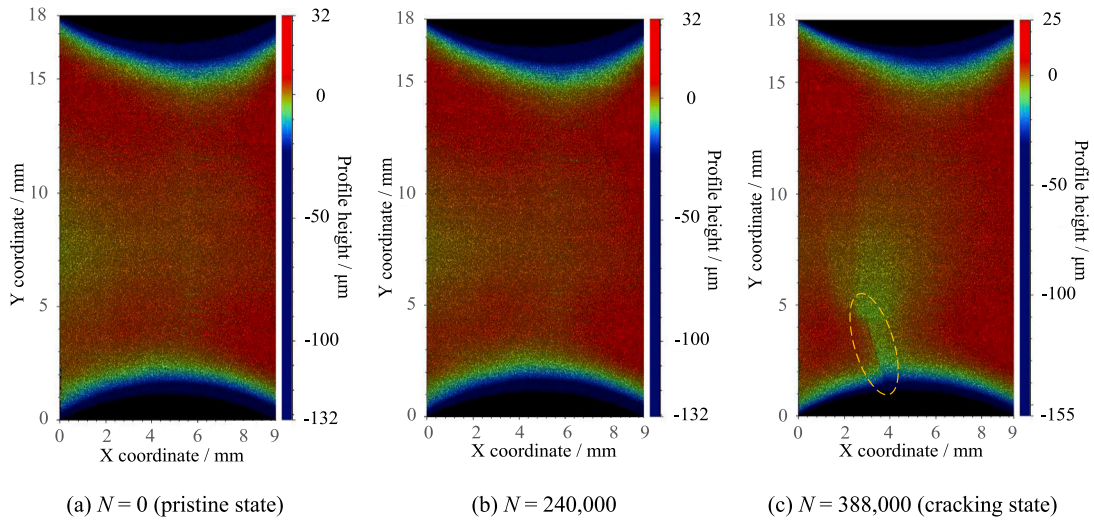


Fig. 15. Contour plots of the surface profile of SR-P-1 at different loading cycles.

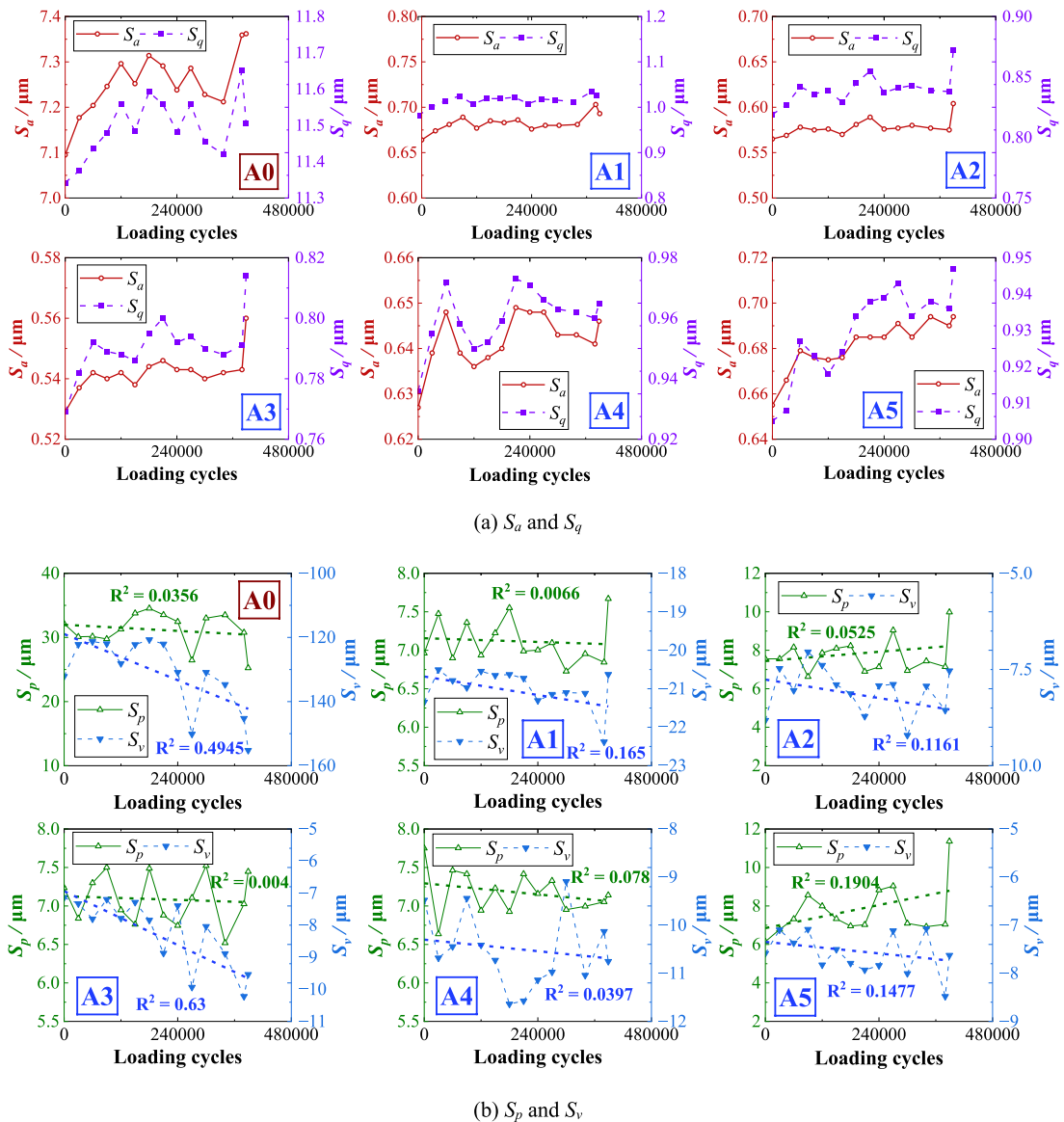
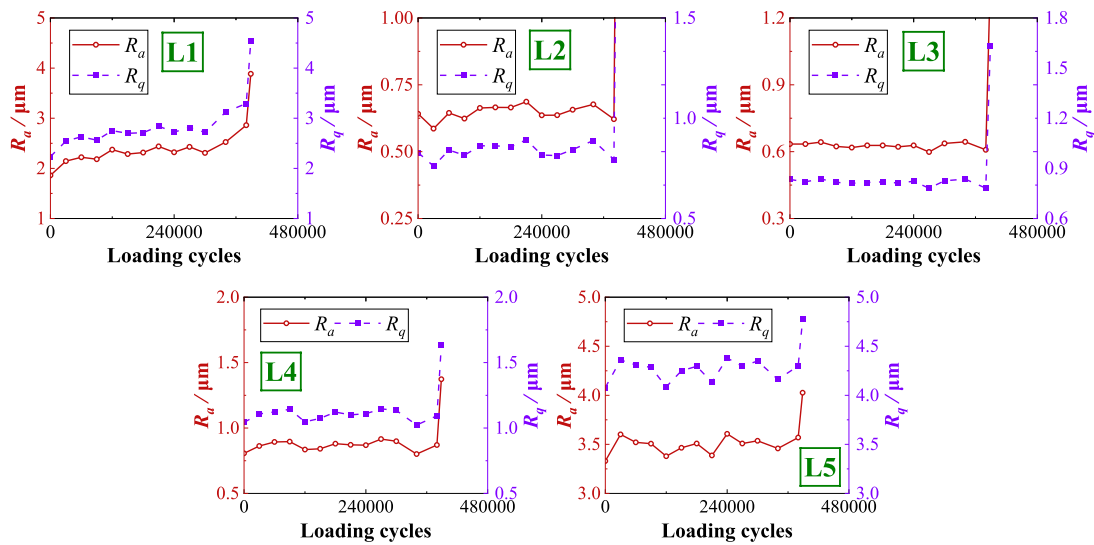
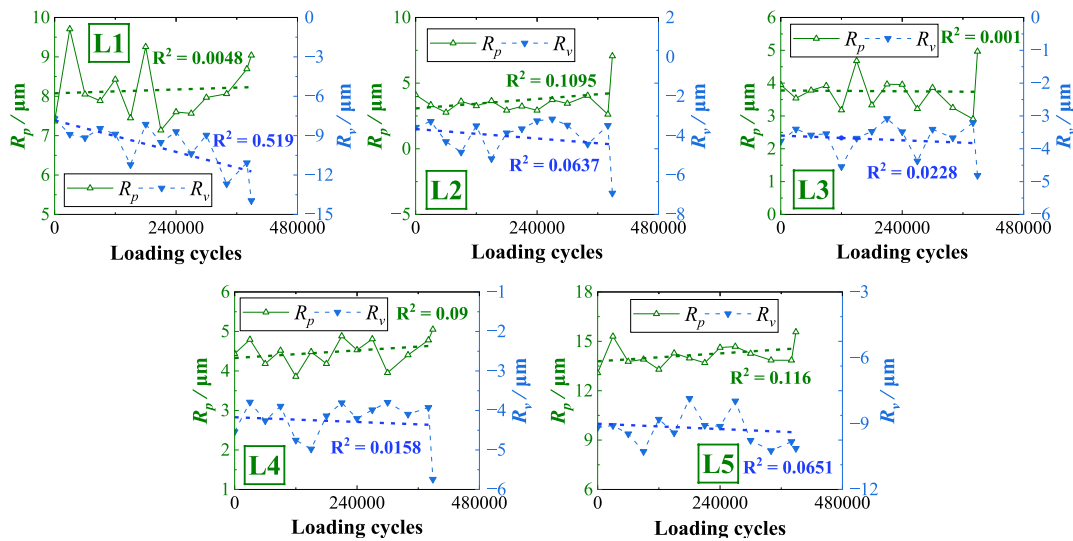


Fig. 16. Evolution of 3D parameters for SR-P-1.



(a)  $R_a$  and  $R_q$



(b)  $R_p$  and  $R_v$

Fig. 17. Evolution of 2D parameters for SR-P-1.

### 3.2.4. SR-P-1

Fig. 15 shows the contour plots of the surface profile of SR-P-1 at different loading cycles. With the loading cycles applied up to 240,000 cycles, no obvious surface profile, height, or peak value changes were observed. When the fatigue crack was initiated (Fig. 15(c)), a concave shape and a height difference along the propagation path were observed.

Fig. 16 shows the evolution of the 3D roughness parameters for specimen SR-P-1. From the evolution results of A1, which is very close to the crack initiation location, it can be seen that both  $S_a$  and  $S_q$  abruptly increase when loaded for 380,000 cycles, just 8,000 cycles earlier than the final cycle, indicating that  $S_a$  and  $S_q$  detect the onset of the fatigue crack in advance compared with manual observation. In this specimen, the evolutions of  $S_a$  and  $S_q$  at A1, A2, and A3 showed a three-phase behavior and reacted sensitively to crack initiation, although the damage accumulation phase was almost horizontal. As A4 and A5 were far from the initiation location, the changes in  $S_a$  and  $S_q$  in the final loading interval were not distinguishable. For the maximum surface roughness parameters,  $S_v$  exhibited a stronger correlation with the loading cycles than  $S_p$  at A1, A2, and A3.

Fig. 17 shows the evolution of the 2D roughness parameters for

specimen SR-P-1. A three-phase behavior of the evolution of  $R_a$  and  $R_q$  was shown at L1, whereas no apparent damage accumulation was found for the other locations. This is reasonable because the surface near the crack initiation location has larger extrusions and intrusions that initiate fatigue cracks, resulting in a sensitive increase in the surface roughness parameters. A similar phenomenon was observed in the maximum surface roughness parameters; only at A1 did the  $R_v$  have a relatively strong correlation with the loading cycles. This can also be attributed to intrusion being the main contributor to fatigue crack initiation [40].

### 3.2.5. SR-P-2

Fig. 18 shows the contour plots of the surface profile of SR-P-2 at different loading cycles. In contrast to the cases in which the load ratio was 0.1, the concavity formed at the crack tip in this specimen had a smaller area and depth. Also, the valley depth decreases from  $-104 \mu\text{m}$  to  $-89 \mu\text{m}$  after applying 560,000 loading cycles, which shows a different tendency compared to SR-P-1.

Fig. 19 shows the evolution of the 3D roughness parameters of SR-P-2. It can be observed that the evolutions of  $S_a$  and  $S_q$  at A1, A2, and A3 exhibit irregular fluctuation within a range of  $\pm 0.005 \mu\text{m}$ , and no

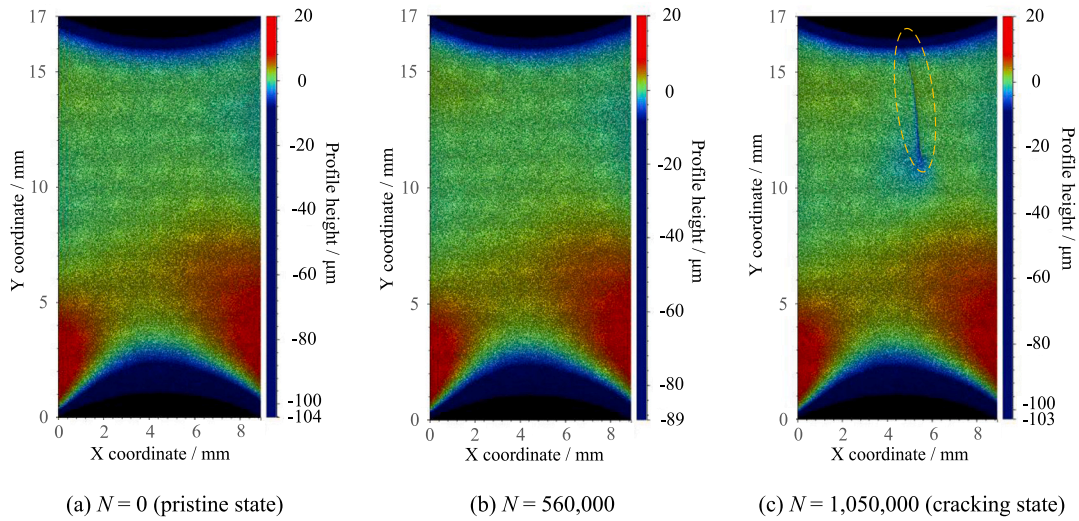


Fig. 18. Contour plots of the surface profile of SR-P-2 at different loading cycles.

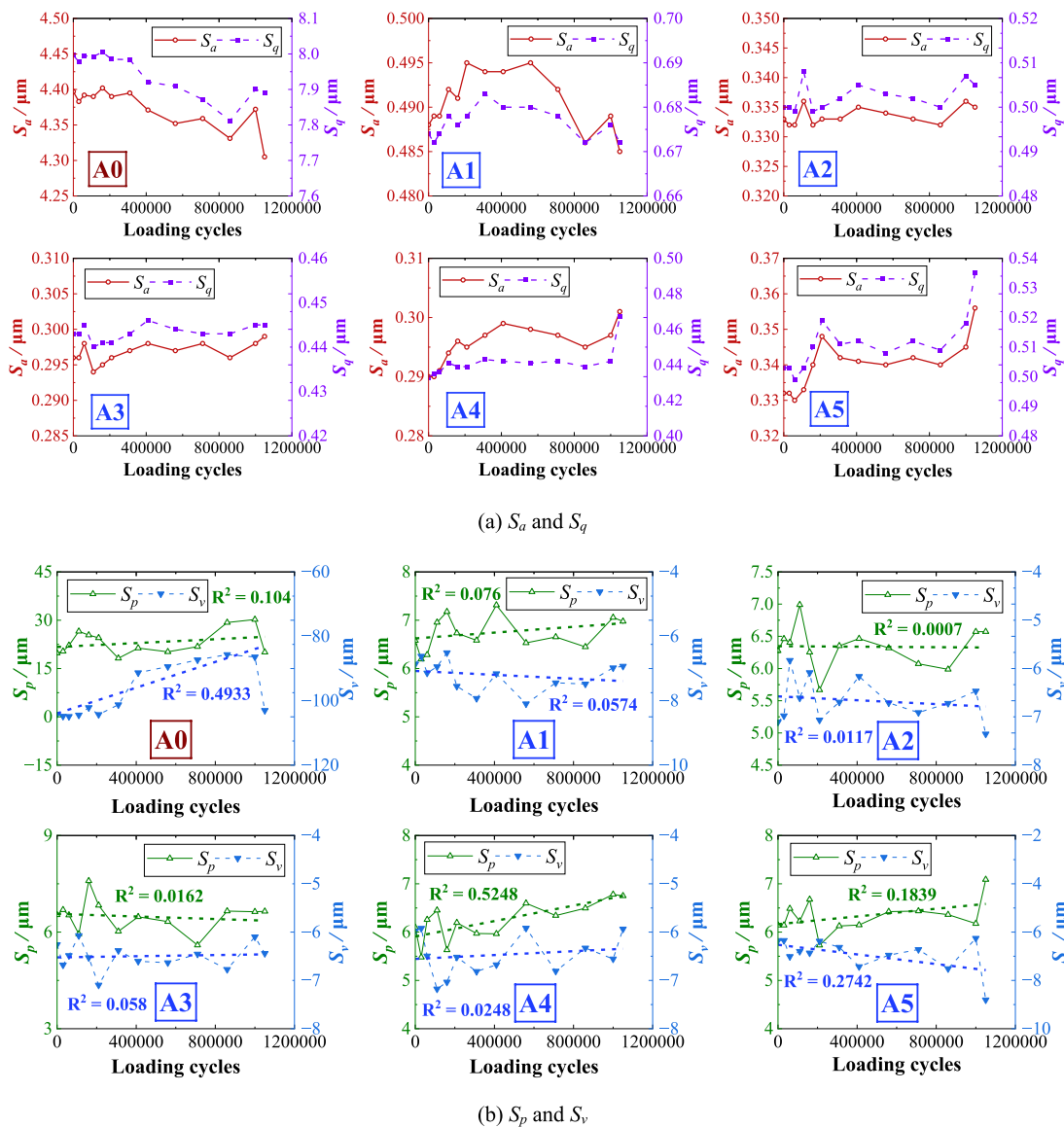
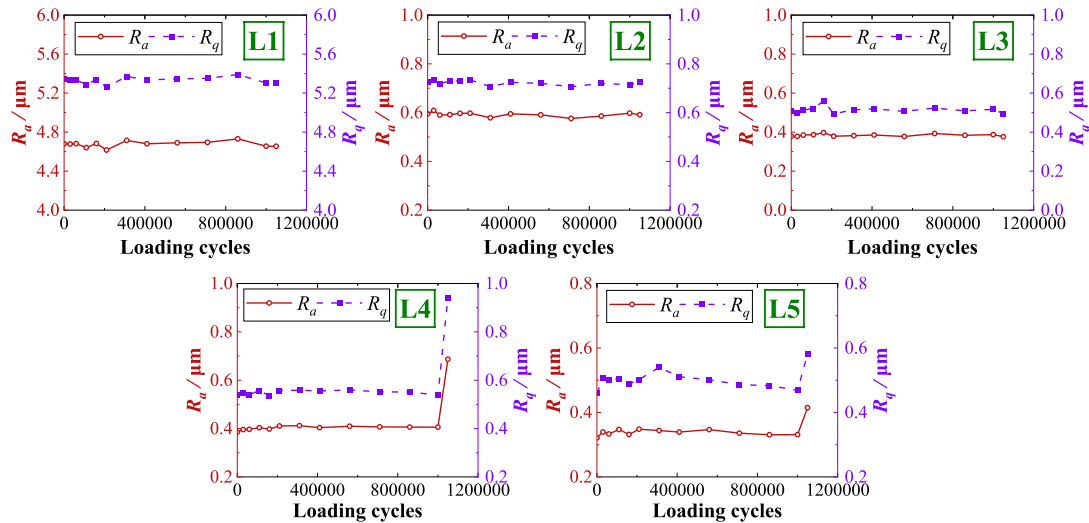
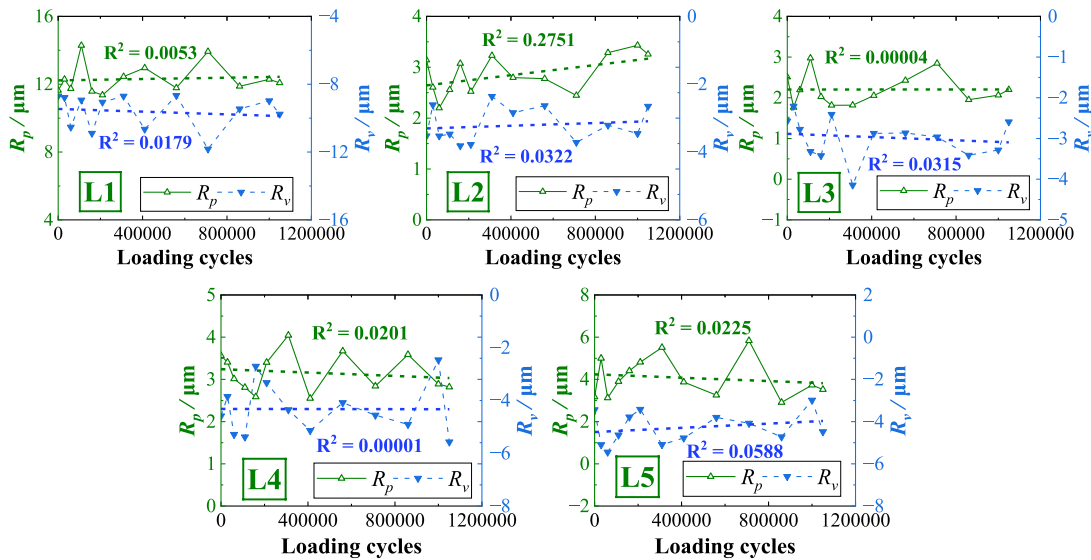


Fig. 19. Evolution of 3D parameters for SR-P-2.



(a)  $R_a$  and  $R_q$



(b)  $R_p$  and  $R_v$

Fig. 20. Evolution of 2D parameters for SR-P-2.

sensitive response of the fatigue crack is found in these areas. However, the evolutions of  $S_a$  and  $S_q$  at A4 and A5 present a familiar three-phase behavior, and the amount of change in value is two times or more, which indicates that  $S_a$  and  $S_q$  react sensitively to fatigue loading at locations where fatigue cracks are about to be initiated. In the case of  $S_p$  and  $S_v$ ,  $S_v$  still had a higher correlation with loading cycles than the others at A5.

Fig. 20 shows the evolution of the 2D roughness parameters for specimen SR-P-2. On the lines far from the crack initiation location, the evolution of  $R_a$  and  $R_q$  remained approximately constant during the entire loading procedure. On L4, though the instant response and damage accumulation phases were not obvious, abrupt increases caused by crack initiation were observed. A rapid increase in  $R_a$  and  $R_q$  in the first loading interval can be observed at L5, which roughly shows three-phase behavior. Neither  $R_p$  nor  $R_v$  can build a strong correlation with the loading cycles, even on the lines near the crack initiation location.

### 3.2.6. SR-P-3

Fig. 21 shows the contour plots of the surface profile of SR-P-3 at

different loading cycles. Because the fatigue loading in this specimen was compression-dominant, the fatigue crack was difficult to observe, and neither the concavity around the crack tip nor the height difference along the crack propagation path was observed, as shown in Fig. 21(c).

Fig. 22 shows the evolution of the 3D roughness parameters for specimen SR-P-3. It is clear from Fig. 22(a) that only at A4 and A5,  $S_a$  and  $S_q$  exhibit an abrupt increase due to fatigue crack initiation, whereas in the remaining three areas, no such response is observed. However, it can also be seen that in all areas, there is a rough tendency to drop during the early stage of fatigue loading, which might be due to excessive compressive stress. After decreasing, a roughly horizontal curve with minor fluctuations was observed. Fig. 22(b) shows that  $S_p$  and  $S_v$  are almost independent of the loading cycles, meaning neither  $S_p$  nor  $S_v$  can indicate the crack initiation location in a compression-dominant fatigue loading procedure.

Fig. 23 shows the evolution of the 2D roughness parameters of SR-P-3. Similar to the evolution of  $S_a$  and  $S_q$  at A5, a decrease – flat – abrupt increase in the evolution patterns of  $R_a$  and  $R_q$  reappears at L4 and L5.

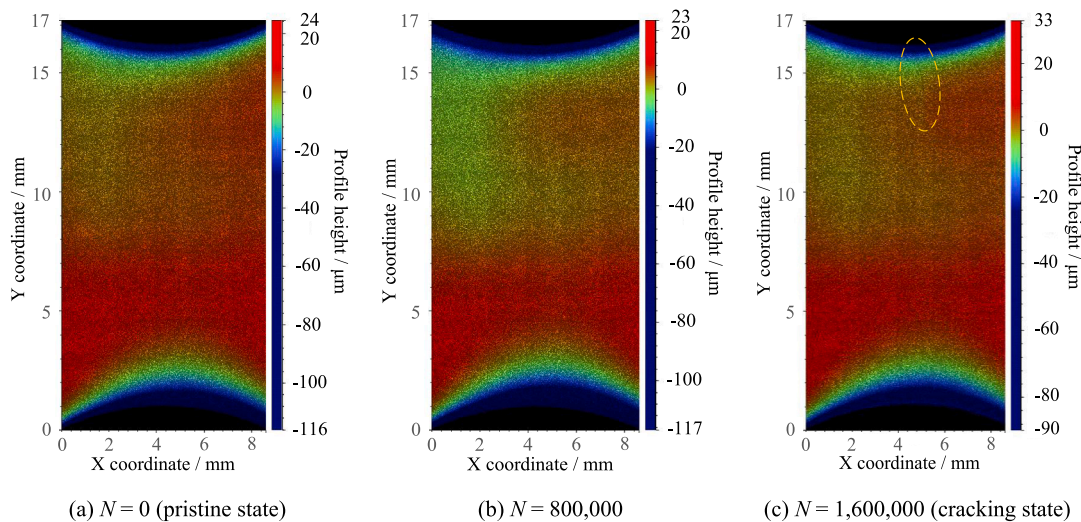
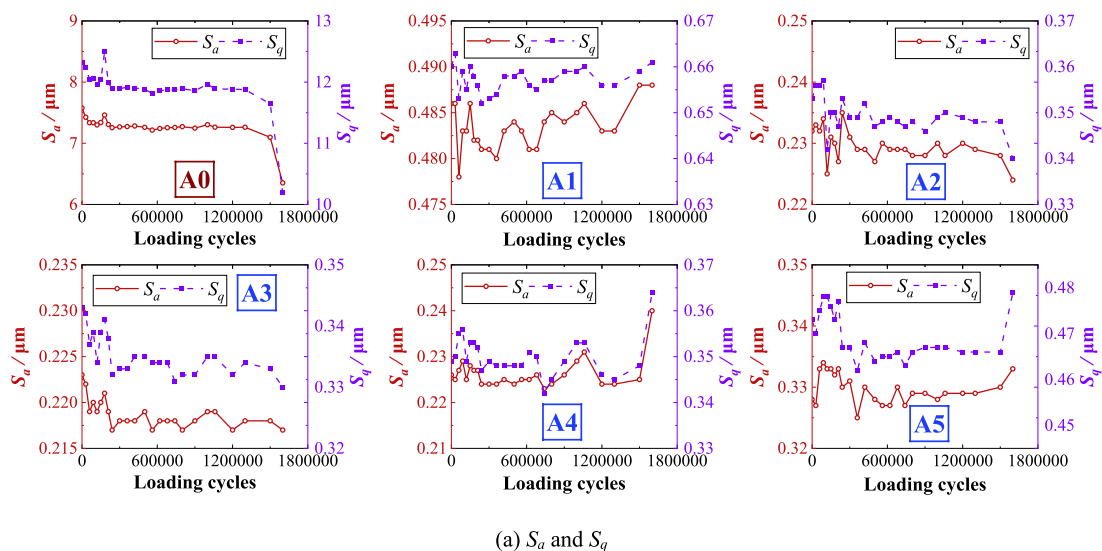
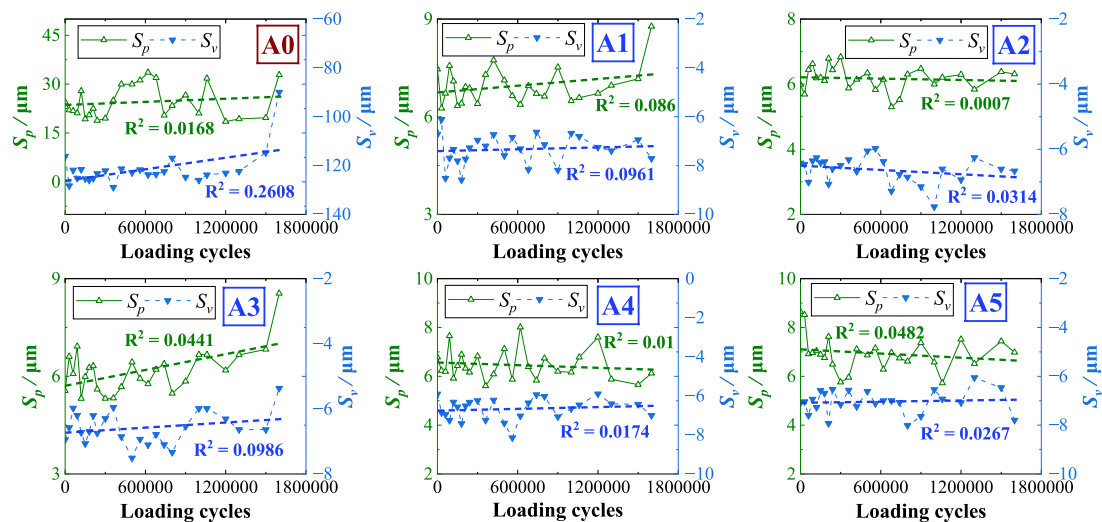


Fig. 21. Contour plots of the surface profile of SR-P-3 at different loading cycles.



(a)  $S_a$  and  $S_q$



(b)  $S_p$  and  $S_v$

Fig. 22. Evolution of 3D parameters for SR-P-3.

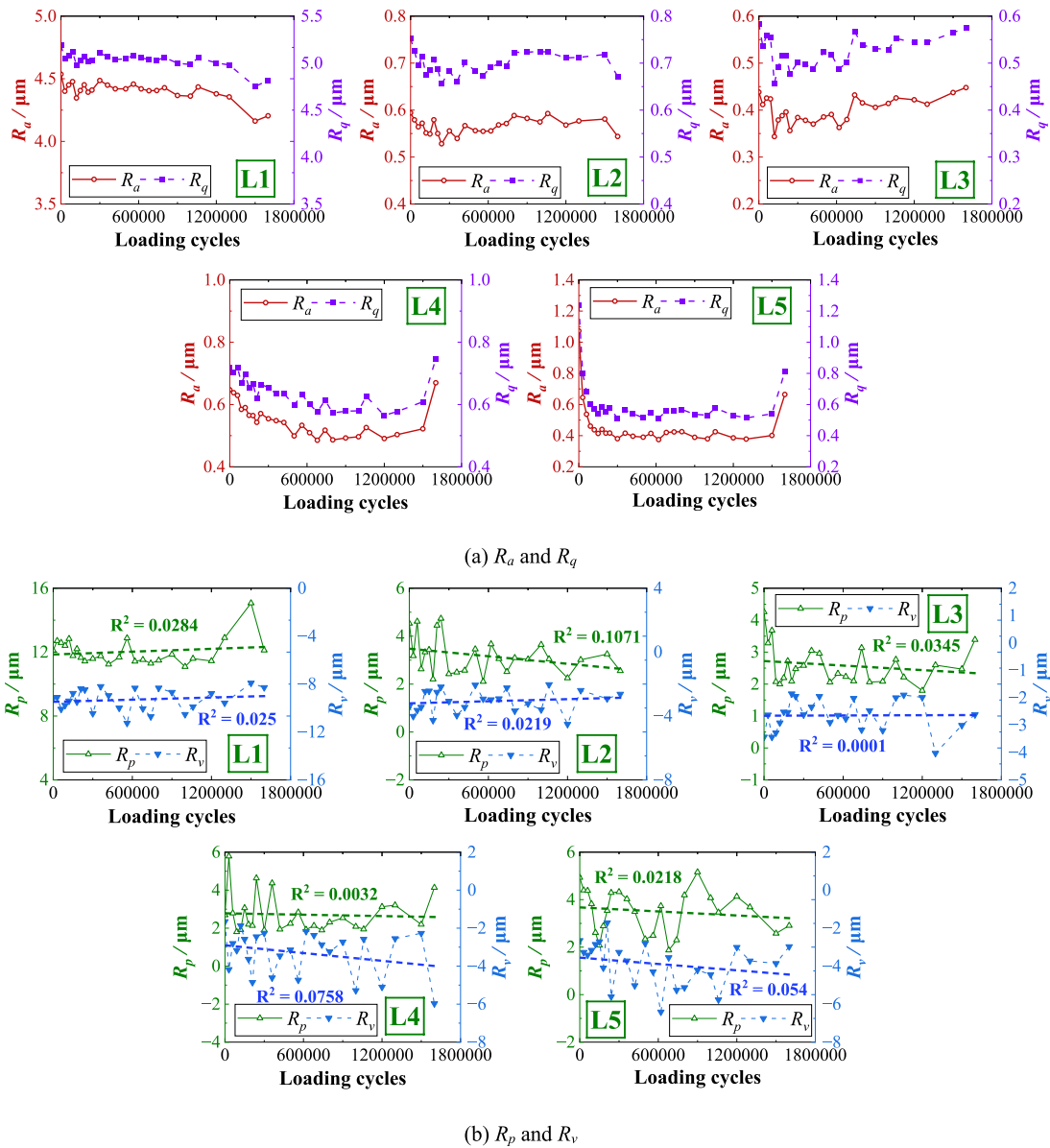


Fig. 23. Evolution of 2D parameters for SR-P-3.

This indicates that the statistical surface roughness parameters may decrease with the application of excessive compressive stress during the early stages of fatigue loading. As for  $R_p$  and  $R_v$ , which are shown in Fig. 23(b), neither shows any tendencies of strong correlation with loading cycles, which is the same as  $S_p$  and  $S_v$  in this specimen.

3.3. Discussion on the results

Based on the aforementioned results, the characteristics of the surface roughness evolution were affected by the initial surface finish and load ratio. In addition, the effects of the sampling region on surface roughness parameters were investigated.

3.3.1. Effect of the initial surface finish

From the measurement results of MR-U and MR-P (or SR-U and SR-P-1), it can be observed that regarding the evolution of the surface parameters  $S_a$  and  $S_q$  for the polished specimens, the rate of change in the damage accumulation phase is lower than that of the corresponding unpolished specimens, which indicates that polishing decreases the rate of change in the damage accumulation phase. This might be due to

eliminating the deep valleys or high peaks, contributing to 3D statistical surface roughness parameter increases. However, for  $R_a$  and  $R_q$ , after polishing, it was easier to observe the damage accumulation phase owing to the optimization effect of the polishing process [26]. Therefore, to make the damage accumulation phase more obvious, it is recommended to have the surface polished for evaluation using 2D surface roughness parameters. For evaluation using 3D surface roughness parameters, surface polishing is not mandatory.

3.3.2. Effect of the load ratio

From the SR-P-1, SR-P-2, and SR-P-3 measurement results, it can be observed that, with the load ratio varying from 0.1 to -1, then to 10 (i. e., from tension-tension loading to tension-compression loading, then to compression-compression loading), the evolutions of the maximum surface roughness parameters have a weaker correlation with the loading cycles. In addition, the evolution pattern of the 3D statistical surface roughness parameters depended on the load ratio. When the load ratio was 0.1, the evolution patterns of  $S_a$  and  $S_q$  exhibited a clear three-phase behavior. When the load ratio is -1, the instant response and damage accumulation phases cannot be clearly observed (except for the

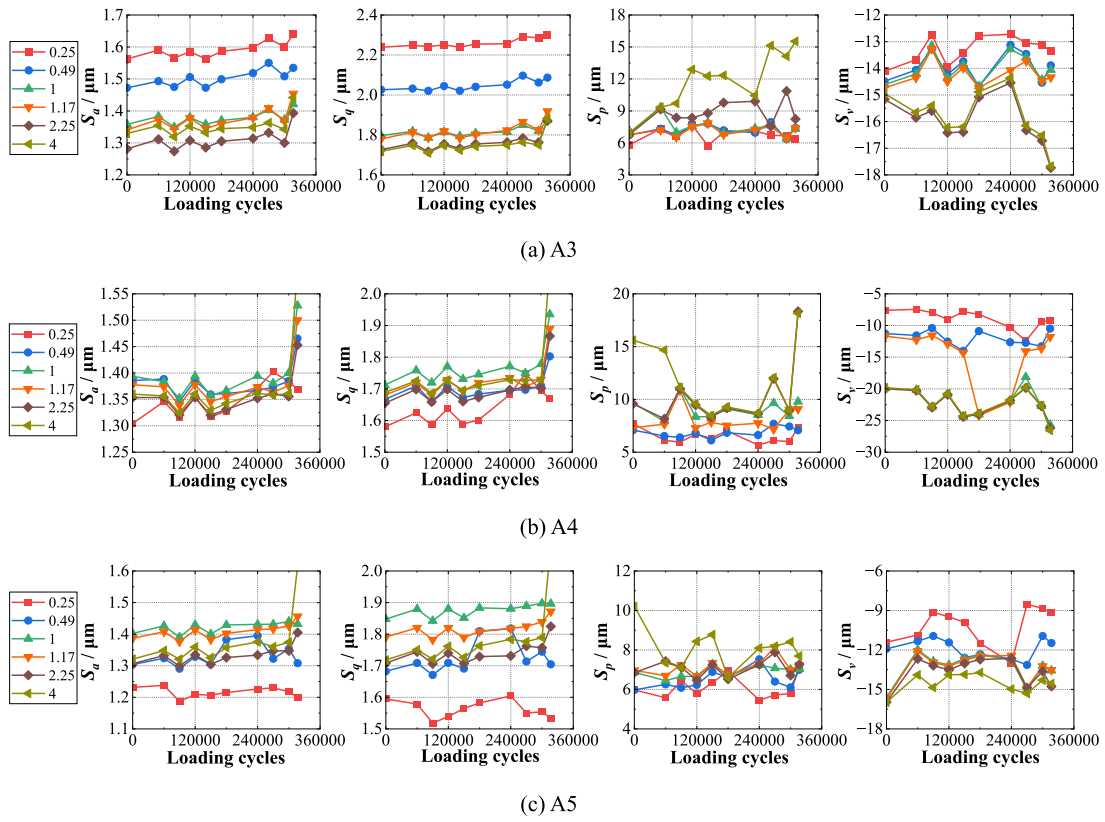


Fig. 24. Comparison of 3D parameters of SR-U using different sampling areas.

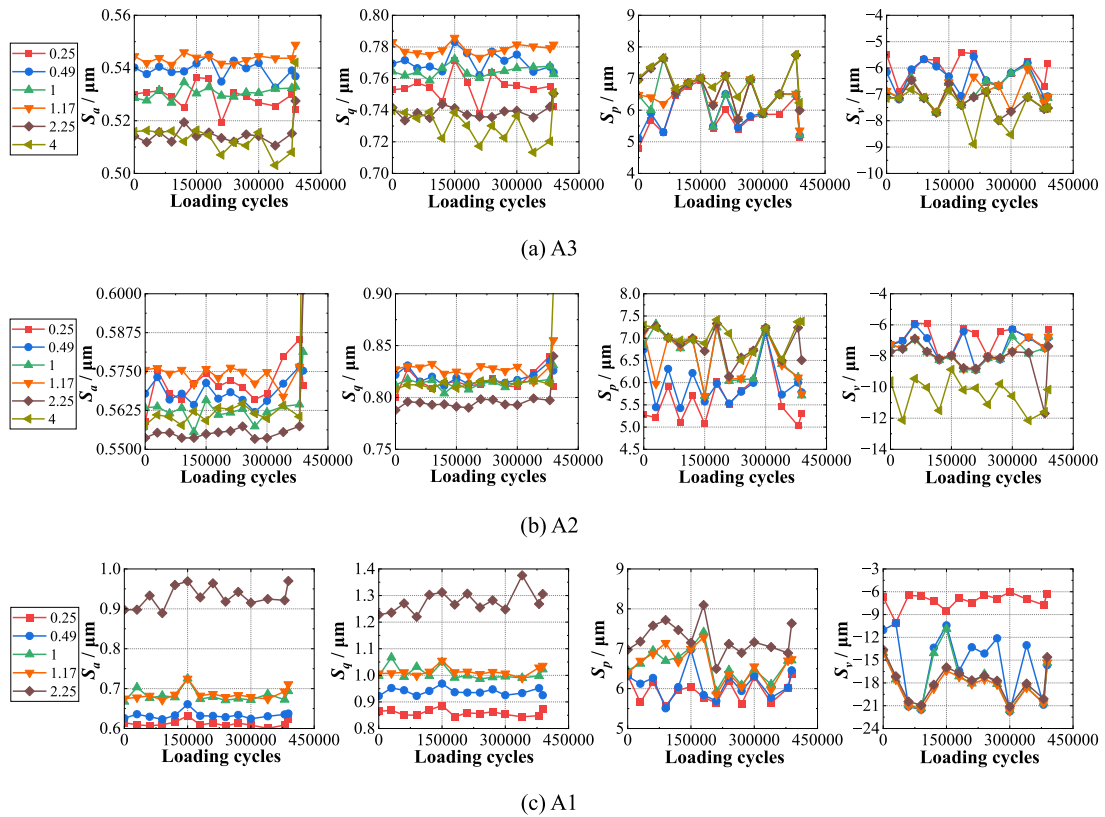


Fig. 25. Comparison of 3D parameters of SR-P-1 using different sampling areas.

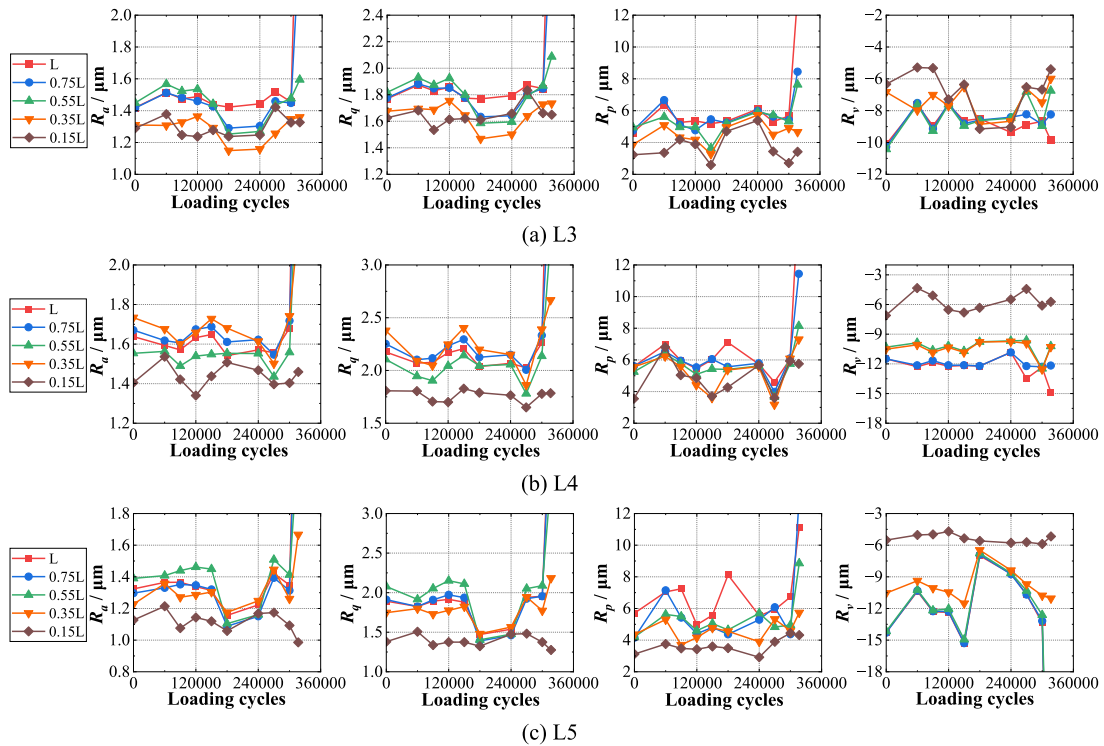


Fig. 26. Comparison of 2D parameters of SR-U using different sampling lengths.

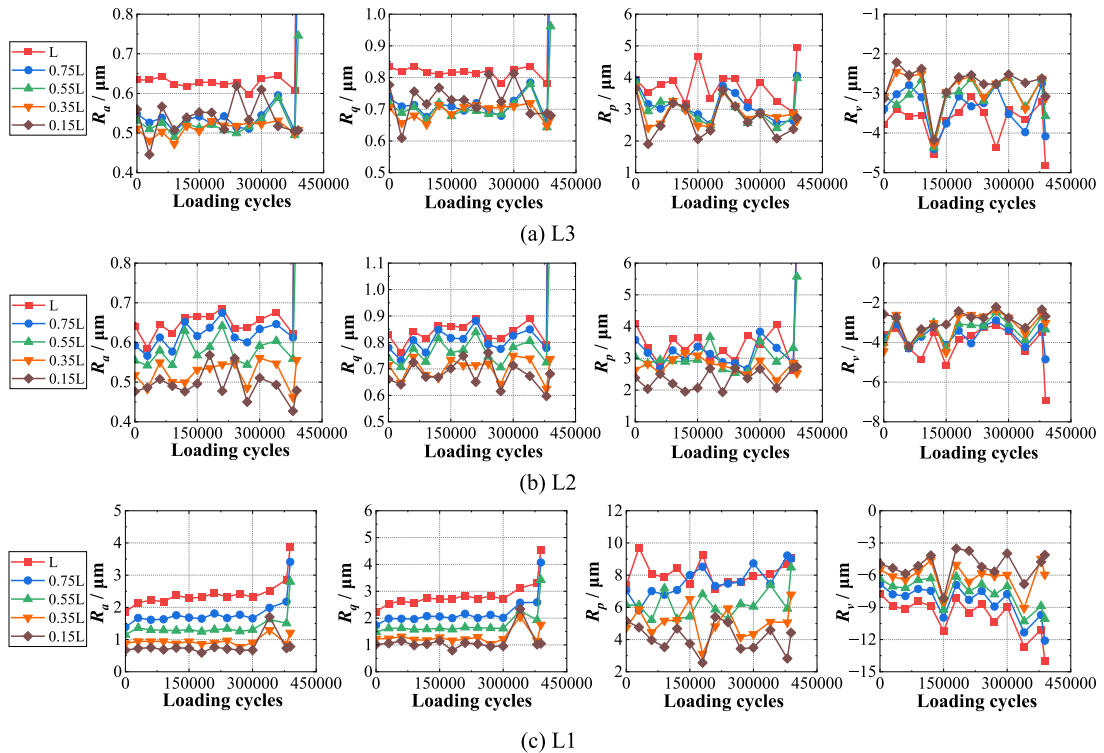


Fig. 27. Comparison of 2D parameters of SR-P-1 using different sampling lengths.

region near the fatigue crack initiation location). When the load ratio was 10, there was a decreasing trend in the instant response phase, which showed the opposite behavior compared to the case with a load ratio of 0.1. In addition,  $S_a$  and  $S_q$  showed no obvious increase with the load cycles in the damage accumulation phase. However, the load ratio does not affect the third phase in each case, which indicates that  $S_a$  and

$S_q$  can capture the fatigue crack initiation regardless of the change in the load ratio, proving that they are better candidates for fatigue crack detection using surface roughness parameters.

### 3.3.3. Effect of the sampling region

A sampling region should be specified in surface roughness

measurements; however, its effects on the surface roughness parameters are still not clear, and the choice of sampling region does not have a widely adopted standard or recommendation. It was reported in [23] that the size of the sampling region has no appreciable effect on the measurement if the critical region, where the maximum stress is located, and fatigue cracks are highly anticipated to initiate, is included. However, in this study, if different regions were used, the surface roughness parameters changed accordingly, as shown in Fig. 6(a) and Fig. 10(a). The measurement results obtained from different sampling regions were compared using parametric studies to study the effects of the sampling region on the surface roughness parameters, as shown in Fig. 24, Fig. 25, Fig. 26 and Fig. 27. SR-U and SR-P-1 were selected for simplification.

First, parametric analyses of 3D parameters were performed, and the five different sampling areas were  $0.5 \times 0.5 \text{ mm}^2$ ,  $0.7 \times 0.7 \text{ mm}^2$ ,  $1 \times 1 \text{ mm}^2$ ,  $1.5 \times 1.5 \text{ mm}^2$ ,  $2 \times 2 \text{ mm}^2$ . Comparisons of the surface roughness evolutions derived from these areas were made for SR-U, as shown in Fig. 24. With an increase in the sampling area, the statistical surface roughness parameters  $S_a$  and  $S_q$  decreased at A3, remained stable at A4, increased before the sampling area reached  $1 \text{ mm}^2$  and stabilized at A5. While for maximum surface roughness parameters  $S_p$  and  $S_v$ , their absolute values increased with the sampling area. The comparison shows that the  $S_a$  and  $S_q$  become stable after the sampling area reaches  $1 \text{ mm}^2$  and the variation range is within  $\pm 5\%$ .

The same parametric study was conducted for SR-P-1, as shown in Fig. 25. At A1, there was a speck of dust with a diameter of around  $10 \mu\text{m}$  attached to the surface during the measurement, and it was covered by the region of  $2 \times 2 \text{ mm}^2$  but not the  $1.5 \times 1.5 \text{ mm}^2$ . As it was larger than the peak height of the surface, the derived surface roughness significantly increased. Thus, the  $2 \times 2 \text{ mm}^2$  results were removed from the comparison shown in Fig. 25(c). With an increase in the sampling area, the statistical surface roughness parameters  $S_a$  and  $S_q$  fluctuated slightly at A3 and remained stable at A2 but increased at A1. While for maximum surface roughness parameters  $S_p$  and  $S_v$ , their absolute values increased with the sampling area. The comparison shows that the  $S_a$  and  $S_q$  become stable after the sampling area reaches  $2.25 \text{ mm}^2$  and the variation range is within  $\pm 5\%$ .

Secondly, the parametric analyses on 2D parameters are conducted for SR-U, and four different sampling lengths, which are  $0.75 L = 6.45 \text{ mm}$ ,  $0.55 L = 4.73 \text{ mm}$ ,  $0.35 L = 3.01 \text{ mm}$ ,  $0.15 L = 1.29 \text{ mm}$ , are selected. A comparison of the surface roughness evolution derived from these regions is shown in Fig. 26. It can be observed that with an increase in the sampling length, the statistical surface roughness parameters  $R_a$  and  $R_q$  increase and tend to be stable after  $4.73 \text{ mm}$ . The maximum surface roughness parameters  $R_p$  and  $R_v$  also show an increasing trend with increasing sampling length, but no consistent convergent limit can be found from L3 to L1.

The same parametric study was conducted for SR-P-1, as shown in Fig. 27. With an increase in the sampling length, all the surface roughness parameters increased monotonically, and the rate of increase was approximately linear. The monotonic increase in the statistical surface roughness parameters  $R_a$  and  $R_p$  was more evident at L1 and L2 than at L3, which can be accounted for by the irreversible surface roughness change caused by the plastic deformation developed around the notch root (see Fig. 2(a)). According to [22], the change in the surface height due to plastic deformation is significantly greater than that due to elastic deformation, and the height change is not uniform owing to the anisotropic characteristics of the surface grains. This indicates that a longer sampling length results in a more diverse change in the surface roughness, resulting in a higher surface roughness value. As for  $R_v$ , the vertical deformation (normal direction of the surface) at L1 was larger than that at L2 and L3 and presented a sagging distribution along the sampling length. Because the calculation of  $R_v$  is based on the average value of all data points, the shorter the sampling length, the lower the absolute value of  $R_v$ .

In conclusion, all the maximum surface roughness parameters (both 2D and 3D) increased with the sampling region, regardless of the level of

stress and the initial surface finish. In the case of the statistical surface roughness parameters,  $S_a$  and  $S_q$  tended to be stable after the sampling area reached a certain value ( $2.25 \text{ mm}^2$  in this study), but  $R_a$  and  $R_q$  only exhibited a tendency to be stable when the surface was unpolished and the sampling length reaches  $4.73 \text{ mm}$ .

#### 4. Conclusions

An experimental study on the surface roughness evolution of steel specimens subjected to fatigue loading is presented herein. The effects of surface polishing and load ratio on surface roughness evolution were quantitatively studied. In addition, the sensitivity of surface roughness measurements to the sampling region was explored by conducting parametric studies. Based on the results of this study, the following conclusions were made:

- (1) Compared with the 2D surface roughness parameters  $R_a$  and  $R_q$ ,  $S_a$  and  $S_q$  are preferable for detecting the onset of fatigue cracks, and their evolution patterns during fatigue loading can be classified into three phases: instant response, damage accumulation, and crack-induced response.
- (2)  $S_v$  effectively indicates the fatigue crack initiation location, except in compression-dominant fatigue loading cases. It has a stronger correlation with the loading cycles when the measured region is close to the initiation location of the fatigue crack.
- (3) Surface polishing makes the damage accumulation of  $R_a$  and  $R_q$  more obvious while having a limited influence on  $S_a$  and  $S_q$ . Therefore, it is recommended to polish the surface for evaluation with 2D statistical surface roughness parameters, and for evaluation with 3D statistical surface roughness parameters, surface polishing is not mandatory.
- (4) The load ratio affects the evolution pattern of the 3D statistical surface roughness parameters. When the load ratio was  $0.1$ , the evolution pattern exhibited a clear three-phase behavior. When the load ratio is  $-1$ , the instant response and damage accumulation phases cannot be clearly observed except for the region near the fatigue crack initiation location. When the load ratio was  $10$ , the instant response phase tended to decrease.
- (5) All 2D surface roughness parameters and 3D maximum surface roughness parameters increased with the sampling region, regardless of the level of stress and initial surface finish, and no tendency of convergence was observed.  $S_a$  and  $S_q$  increased with the sampling area and tended to be stable after the sampling area reaches a certain value ( $2.25 \text{ mm}^2$  in this study).

#### CRedit authorship contribution statement

**Rui Hao:** Conceptualization, Methodology, Investigation, Writing – original draft, Visualization. **Weiwei Lin:** Funding acquisition, Conceptualization, Methodology, Supervision, Writing – review & editing.

#### Declaration of Competing Interest

The authors declare the following financial interests/personal relationships which may be considered as potential competing interests: Weiwei Lin reports financial support was provided by Jane and Aatos Erkkö Foundation. Weiwei Lin reports financial support was provided by Aalto University.

#### Acknowledgement

This research was partially sponsored by the Jane and Aatos Erkkö Foundation in Finland (Grant No. 210018) and the Aalto research project funding in ENG 2022. The support provided by Dr Pauli Lehto and Mr Kim Widell in the guidance of the measurement equipment and

Dr Youqi Zhang in guiding the Python coding is also appreciated.

## References

- [1] Salam I, Tauqir A, Ul Haq A, Khan AQ. An air crash due to fatigue failure of a ball bearing. *Eng Fail Anal* 1998;5(4):261–9. <https://doi.org/10.1016/B978-0-08-043959-4.50042-0>.
- [2] Botny R, Kaleta J. A method for determining the heat energy of the fatigue process in metals under uniaxial stress: Part 1. Determination of the amount of heat liberated from a fatigue-tested specimen. *Int J Fatigue* 1986;8(1):29–33. [https://doi.org/10.1016/0142-1123\(86\)90044-7](https://doi.org/10.1016/0142-1123(86)90044-7).
- [3] Xin H, Veljkovic M. Fatigue crack initiation prediction using phantom nodes-based extended finite element method for S355 and S690 steel grades. *Eng Fract Mech* 2019;214:164–76. <https://doi.org/10.1016/j.engfracmech.2019.04.026>.
- [4] Itoga H, Tokaji K, Nakajima M, Ko HN. Effect of surface roughness on step-wise S-N characteristics in high strength steel. *Int J Fatigue* 2003;25:379–85. [https://doi.org/10.1016/S0142-1123\(02\)00166-4](https://doi.org/10.1016/S0142-1123(02)00166-4).
- [5] Alang NA, Razak NA, Miskam AK. Effect of surface roughness on fatigue life of notched carbon steel. *Int J Eng Technol IJET-IJENS* 2011;11:160–3.
- [6] Saberifar S, Mashreghi AR, Mosalaeepour M, Ghasemi SS. The interaction between non-metallic inclusions and surface roughness in fatigue failure and their influence on fatigue strength. *Mater Des* 2012;35:720–4. <https://doi.org/10.1016/j.matdes.2011.10.028>.
- [7] Lai J, Huang H, Busing W. Effects of microstructure and surface roughness on the fatigue strength of high-strength steels. *Procedia Struct Integr* 2016;2:1213–20. <https://doi.org/10.1016/j.prostr.2016.06.155>.
- [8] Gockel J, Sheridan L, Koerper B, Whip B. The influence of additive manufacturing processing parameters on surface roughness and fatigue life. *Int J Fatigue* 2019;124:380–8. <https://doi.org/10.1016/j.ijfatigue.2019.03.025>.
- [9] Shrestha R, Samsirwong J, Shamsaei N. Fatigue behavior of additive manufactured 316L stainless steel parts: Effects of layer orientation and surface roughness. *Addit Manuf* 2019;28:23–38. <https://doi.org/10.1016/j.addma.2019.04.011>.
- [10] Maiya PS, Busch DE. Effect of surface roughness on low-cycle fatigue behavior of Type 304 stainless steel. *Metall Trans A* 1975;6A:1761–6. <https://doi.org/10.1007/BF02642305>.
- [11] Xiao WL, Chen HB, Yin Y. Effects of surface roughness on the fatigue life of alloy steel. *Key Eng Mater* 2012;525–526:417–20. <https://doi.org/10.4028/www.scientific.net/KEM.525-526.417>.
- [12] Wang J, Zhang Y, Sun Q, Liu S, Shi B, Lu H. Giga-fatigue life prediction of FV520B-I with surface roughness. *Mater Des* 2016;89:1028–34. <https://doi.org/10.1016/j.matdes.2015.10.104>.
- [13] Li C, Dai W, Duan F, Zhang Y, He D. Fatigue life estimation of medium-carbon steel with different surface roughness. *Appl Sci* 2017;7:1–11. <https://doi.org/10.3390/app7040338>.
- [14] Bohacova M. Methodology of short fatigue crack detection by the eddy current method in a multi-layered metal aircraft structure. *Eng Fail Anal* 2013;35:597–608. <https://doi.org/10.1016/j.engfailanal.2013.06.009>.
- [15] Tanaka K. 4.04 – Fatigue crack propagation. *Comprehensive structural integrity*. Pergamon; 2003. p. 95–127.
- [16] Sola JF, Kelton R, Meletis EI, Huang H. A surface roughness based damage index for predicting future propagation path of microstructure-sensitive crack in pure nickel. *Int J Fatigue* 2019;122:164–72. <https://doi.org/10.1016/j.ijfatigue.2019.01.012>.
- [17] Yue Z. Surface roughness evolution under constant amplitude fatigue loading using crystal plasticity. *Eng Fract Mech* 2005;72:749–57. <https://doi.org/10.1016/j.engfracmech.2004.06.001>.
- [18] Ogawa H, Hatanaka K. Quantitative evaluation of surface configuration in fatigued carbon steel in terms of AFM observations. *Trans JSME (in Japanese)* 2002;68(665):57–64. <https://doi.org/10.1299/kikaia.68.57>.
- [19] Hussein AM, El-Awady JA. Surface roughness evolution during early stages of mechanical cyclic loading. *Int J Fatigue* 2016;87:339–50. <https://doi.org/10.1016/j.ijfatigue.2016.02.022>.
- [20] Wang Y, Meletis E, Huang H. Quantitative study of surface roughness evolution during low-cycle fatigue of 316L stainless steel using Scanning Whitelight Interferometric (SWLI) Microscopy. *Int J Fatigue* 2013;48:280–8. <https://doi.org/10.1016/j.ijfatigue.2012.11.009>.
- [21] Lacerda JC, Martins GD, Signoretto VT, Teixeira RLP. Evolution of the surface roughness of a low carbon steel subjected to fatigue. *Int J Fatigue* 2017;102:143–8. <https://doi.org/10.1016/j.ijfatigue.2017.05.010>.
- [22] Tada N, Uemori T. Microscopic elastic and plastic inhomogeneous deformations and height changes on the surface of a polycrystalline pure-titanium plate specimen under cyclic tension. *Appl Sci* 2018;8. <https://doi.org/10.3390/app8101907>.
- [23] Haghshenas A, Khonsari MM. Damage accumulation and crack initiation detection based on the evolution of surface roughness parameters. *Int J Fatigue* 2018;107:130–44. <https://doi.org/10.1016/j.ijfatigue.2017.10.009>.
- [24] Sola FJ, Kelton R, Meletis EI, Huang H. Predicting crack initiation site in polycrystalline nickel through surface topography changes. *Int J Fatigue* 2019;124:70–81. <https://doi.org/10.1016/j.ijfatigue.2019.02.027>.
- [25] Kelton R, Fathi J, Meletis EI, Huang H. Study of the surface roughness evolution of pinned fatigue cracks, and its relation to crack pinning duration and crack propagation rate between pinning points. *ASME Int Mech Eng Congr Expo Proc* 2017;9:1–5. <https://doi.org/10.1115/IMECE2017-70729>.
- [26] Yao C, Wu D, Ma L, Tan L, Zhou Z, Zhang J. Surface integrity evolution and fatigue evaluation after milling mode, shot-peening and polishing mode for TB6 titanium alloy. *Appl Surf Sci* 2016;387:1257–64. <https://doi.org/10.1016/j.apusc.2016.06.162>.
- [27] Haghshenas A, Khonsari MM. On the removal of extrusions and intrusions via repolishing to improve metal fatigue life. *Theor Appl Fract Mech* 2019;103:102248. <https://doi.org/10.1016/j.tafmec.2019.102248>.
- [28] Di J, Ruan X, Zhou X, Wang J, Peng X. Fatigue assessment of orthotropic steel bridge decks based on strain monitoring data. *Eng Struct* 2021;228:111437. <https://doi.org/10.1016/j.engstruct.2020.111437>.
- [29] Xin H, Correia JAF, Veljkovic M. Three-dimensional fatigue crack propagation simulation using extended finite element methods for steel grades S355 and S690 considering mean stress effects. *Eng Struct* 2021;227:111414. <https://doi.org/10.1016/j.engstruct.2020.111414>.
- [30] Zhu Z, Li J, Huang Y, Carpinteri A. Hot-spot stress models of cutout detail on orthotropic steel bridge decks. *J Constr Steel Res* 2020;183:106762. <https://doi.org/10.1016/j.jcsr.2021.106762>.
- [31] Yan F, Chen W, Lin Z. Prediction of fatigue life of welded details in cable-stayed orthotropic steel deck bridges. *Eng Struct* 2016;127:344–58. <https://doi.org/10.1016/j.engstruct.2016.08.055>.
- [32] Shi Z, Zhou Y, Sun Z, Yang S. Fatigue performance of orthotropic steel decks in a wide steel-box girder. *J Constr Steel Res* 2022;190:107109. <https://doi.org/10.1016/j.jcsr.2021.107109>.
- [33] Chen Z, Li C, He J, Xin H. Retrofit fatigue cracked diaphragm cutouts using improved geometry in orthotropic steel decks. *Appl Sci* 2020;10:3983. <https://doi.org/10.3390/app10113983>.
- [34] Deng M, Zhang J, Wang R, Yan Y, Dai L, Wang L. Reinforcement of orthotropic steel bridge deck for cable-stayed bridge based on UHPC paving system. *J Chang'an Univ (Nat Sci Ed)* 2018;38:67–74. in Chinese.
- [35] Li M, Hashimoto K, Sugiura K. Influence of asphalt surfacing on fatigue evaluation of rib-to-deck joints in orthotropic steel bridge decks. *J Bridge Eng* 2014;19(10):04014038. [https://doi.org/10.1061/\(ASCE\)JBE.1943-5592.0000610](https://doi.org/10.1061/(ASCE)JBE.1943-5592.0000610).
- [36] Remes H, Korhonen E, Lehto P, Romanoff J, Niemelä A, Hiltunen P, et al. Influence of surface integrity on the fatigue strength of high-strength steels. *J Constr Steel Res* 2013;89:21–9. <https://doi.org/10.1016/j.jcsr.2013.06.003>.
- [37] Zhu Z, Xiang Z, Li J, Carpinteri A. Fatigue damage investigation on diaphragm cutout detail on orthotropic bridge deck based on field measurement and FEM. *Thin-Walled Struct* 2020;157:107106. <https://doi.org/10.1016/j.tws.2020.107106>.
- [38] Surface Texture (Surface Roughness, Waviness, and Lay). New York: American Society of Mechanical Engineers. 2020.
- [39] Meng F, Ferrié E, Déprés C, Fivel M. 3D discrete dislocation dynamic investigations of persistent slip band formation in FCC metals under cyclic deformation. *Int J Fatigue* 2021;149:106234. <https://doi.org/10.1016/j.ijfatigue.2021.106234>.
- [40] Polák J, Man J, Vystavel T. The shape of extrusions and intrusions and initiation of stage I fatigue cracks. *Mater Sci Eng A* 2009;517:204–11. <https://doi.org/10.1016/j.msea.2009.03.070>.
- [41] Hao R, Lehto P, Lin W. Critical distance-based fatigue life evaluation of blunt notch details in steel bridges. *J Constr Steel Res* 2023;201:107738. <https://doi.org/10.1016/j.jcsr.2022.107738>.